Neurobiology of Disease

Modulating the Excitability of Olfactory Output Neurons Affects Whole-Body Metabolism

Louis John Kolling,[1] Roberta Tatti,[2] Troy Lowry,[2] Ashley M. Loeven,[2] James M. Fadool,[2,3] and Debra Ann Fadool[1,2,3]

[1]Institute of Molecular Biophysics, The Florida State University, Tallahassee, Florida 32306, [2]Department of Biological Science, The Florida State University, Tallahassee, Florida 32306, and [3]Program in Neuroscience, The Florida State University, Tallahassee, Florida 32306

Metabolic state can alter olfactory sensitivity, but it is unknown whether the activity of the olfactory bulb (OB) may fine tune metabolic homeostasis. Our objective was to use CRISPR gene editing in male and female mice to enhance the excitability of mitral/tufted projection neurons (M/TCs) of the OB to test for improved metabolic health. *Ex vivo* slice recordings of MCs in CRISPR mice confirmed increased excitability due the targeted loss of Kv1.3 channels, which resulted in a less negative resting membrane potential (RMP), enhanced action potential (AP) firing, and insensitivity to the selective channel blocker margatoxin (MgTx). CRISPR mice exhibited enhanced odor discrimination using a habituation/dishabituation paradigm. CRISPR mice were challenged for 25 weeks with a moderately high-fat (MHF) diet, and compared with littermate controls, male mice were resistance to diet-induced obesity (DIO). Female mice did not exhibit DIO. CRISPR male mice gained less body weight, accumulated less white adipose tissue, cleared a glucose challenge more quickly, and had less serum leptin and liver triglycerides. CRISPR male mice consumed equivalent calories as control littermates, and had unaltered energy expenditure (EE) and locomotor activity, but used more fats for metabolic substrate over that of carbohydrates. Counter to CRISPR-engineered mice, by using chemogenetics to decrease M/TC excitability in male mice, activation of inhibitory designer receptors exclusively activated by designer drugs (DREADDs) caused a decrease in odor discrimination, and resulted in a metabolic profile that was obesogenic, mice had reduced EE and oxygen consumption (VO_2). We conclude that the activity of M/TC projection neurons canonically carries olfactory information and simultaneously can regulate whole-body metabolism.

Key words: CRISPR; Kv1.3; obesity; olfaction; olfactory bulb; potassium channel

Significance Statement

The olfactory system drives food choice, and olfactory sensitivity is strongly correlated to hunger and fullness. Olfactory function thereby influences nutritional balance and obesity outcomes. Obesity has become a health and financial crisis in America, shortening life expectancy and increasing the severity of associated illnesses. It is expected that 51% of Americans will be obese by the year 2030. Using CRISPR gene editing and chemogenetic approaches, we discovered that changing the excitability of output neurons in the olfactory bulb (OB) affects metabolism and body weight stabilization in mice. Our results suggest that long-term therapeutic targeting of OB activity to higher processing centers may be a future clinical treatment of obesity or type II Diabetes.

Received Jan. 19, 2022; revised June 6, 2022; accepted June 8, 2022.

Author contributions: L.J.K., J.M.F., and D.A.F. designed research; L.J.K., R.T., T.L., A.M.L., and D.A.F. performed research; L.J.K., R.T., A.M.L., and D.A.F. analyzed data; L.J.K. and D.A.F. wrote the first draft of the paper; L.J.K., R.T., T.L., J.M.F., A.M.L., and D.A.F. edited the paper; L.J.K. and D.A.F. wrote the paper.

This work was supported by the National Institutes of Health (NIH) Grant T32 DC000044 from the National Institute of Deafness and Communication Disorders, the NIH Grant R01 EY030633 from the National Eye Institute, a Graduate Research Fellowship 2017-240762 from the National Science Foundation, and a United States Department of Agriculture 2019-07151 Predoctoral Fellowship from the National Institute of Food and Agriculture. This work was also supported by a Robinson Endowment Award from Tallahassee Memorial Hospital and a Planning Grant from Florida State University Council of Research and Creativity. Publication costs were supported by the Higher Education Emergency Relief Fund. We thank Ms. Alexis Cox, Ms. Tyla Dolezel, Mr. Aiden Carley, Ms. Carley Huffstetler, and Ms. Abigail Thomas for excellent technical assistance and help with mouse husbandry. We also thank Ms. Camilla May for additional mouse handling and record keeping and Dr. Jennifer Steiner for her metabolic expertise and helpful discussions concerning diet, nutrition, and energetics.

The authors declare no competing financial interests.

Correspondence should be addressed to Debra Ann Fadool at dfadool@bio.fsu.edu.

https://doi.org/10.1523/JNEUROSCI.0190-22.2022

Introduction

The olfactory system is a prominent driver of food choice. Indeed, olfactory sensitivity heavily correlates with feeding state and satiety (Palouzier-Paulignan et al., 2012; Marty et al., 2017; Murphy and Vertrees, 2017; Fadool and Kolling, 2020). While the correlation of metabolic factors to olfactory function is incompletely understood, it is known that olfactory bulb (OB) neurons are modulated in response to metabolically-relevant molecules (Fadool et al., 2000, 2011; Palouzier-Paulignan et al., 2012; Tucker et al., 2013; Kuczewski et al., 2014; Thiebaud et al., 2016; Fadool and Kolling, 2020; Faour et al., 2022). A major driver of neuronal excitability is the family of voltage-gated potassium (Kv) channels that classically act as dampeners of excitability through shaping of the action potential (AP), timing of

the interspike interval (ISI), and stabilizing the resting potential (Jan and Jan, 1994; Yellen, 2002; Kaczmarek, 2006).

Of particular interest in the processing of odor coding within the OB are the mitral and tufted cells (M/TCs) that pass sensory information to other parts of the brain as the primary output projection neurons (Imamura et al., 2020; Jones et al., 2020; Zeppilli et al., 2021). The Kv channel, Kv1.3, carries 60–80% of the outward current in the MCs (Fadool and Levitan, 1998), thereby it has a prominent role in modulating excitability. Changing the biophysical properties of Kv1.3 by using pharmacological blockers, phosphorylation, or introducing neuromodulators of the channel has been well studied, particularly with regards to MC output neurons (Fadool and Levitan, 1998; Tucker and Fadool, 2002; Marks et al., 2009; Fadool et al., 2011; Mast and Fadool, 2012; Tucker et al., 2013; Schwartz et al., 2021). Our objective was to selectively manipulate output neurons using cell-specific genome editing of Kv1.3 to identify how olfactory information processing and whole-body metabolism are interdependent.

It is known that knock-out of the *Kv1.3* gene (global knock-out, Kv1.3−/− mice) causes resistance to diet-induced obesity (DIO); mice are thin with an increase in total energy expenditure (TEE), and they have a "Super-smeller" olfactory phenotype: mice have an increase in odor discrimination and lower odor threshold (Xu et al., 2003, 2004; Fadool et al., 2004; Tucker et al., 2012b). After surgical removal of the OB, which largely induces anosmia, Kv1.3−/− mice are no longer resistant to DIO and they have a reduction in TEE (Tucker et al., 2012a). These effects underscore the relationship between olfaction and metabolic balance; however, global deletion of Kv1.3 does not permit direct determination of the OB's contribution to metabolic balance. Kv1.3 is believed to be expressed in the hypothalamus, a known regulator of whole-body metabolism (Jin and Diano, 2018). Kv1.3 is also highly expressed in skeletal muscle tissue, where it regulates plasma membrane GLUT4 trafficking to aid in glucose homeostasis (Li et al., 2006). Moreover, the channel is expressed in brown adipose tissue where it can regulate β-oxidation of fatty acids to increase EE (Upadhyay et al., 2013). Because of this, we wanted to explore the central contribution of Kv1.3 activity in the OB, to specifically understand this intersection of olfaction and whole-body metabolism.

In the present study, we selectively enhanced or suppressed the electrical activity of M/TC output neurons by taking advantage of the Tbx21-Cre mouse line, which restricts recombinase activity to these neurons (Haddad et al., 2013). We used *in vivo* CRISPR-Cas9 (CRISPR) gene editing to effect conditional gene inactivation of *Kv1.3*, and selectively increase the excitability of M/TCs. CRISPR mice were challenged with a high-fat diet, assessed for olfactory phenotype, and profiled metabolically. The biophysical properties of CRISPR MCs were examined *ex vivo*. Inhibitory designer receptors exclusively activated by designer drugs (DREADDs) were used to oppositely suppress the activity of M/TCs in a separate cohort of mice, which were then tested for change in olfactory discrimination and profiled for metabolic phenotype. These data identify a previously unknown role for projection neurons of the OB, neurons that transfer olfactory information to higher cortical regions while modulating energy homeostasis.

Materials and Methods

Solutions, reagents, and antisera

Human embryonic kidney (HEK 293) bath solution consisted of (in mM): 150 KCl, 10 HEPES, 1 EGTA, and 0.5 $MgCl_2$, pH 7.4. HEK 293 intracellular (pipette) solution consisted of (in mM): 30 KCl, 120 NaCl, 2 $CaCl_2$, and 10 HEPES, pH 7.4. Artificial CSF (aCSF) contained (in mM): 119 NaCl, 26.2 $NaHCO_3$, 1 NaH_2PO_4, 2.5 KCl, 1.3 $MgCl_2$, 2.5 $CaCl_2$ and 22 d-glucose (pH 7.3; 300–310 mOsm). Sucrose-modified aCSF was used for vibratome sectioning and recovery, and contained (in mM): 83 NaCl, 26.2 $NaHCO_3$, 1 NaH_2PO_4, 3.3 $MgCl_2$, 0.5 $CaCl_2$, 72 sucrose and 22 D-glucose (pH 7.3; 300–310 mOsm; De Saint Jan and Westbrook, 2007). Slice intracellular (pipette) solution contained (in mM): 135 potassium gluconate, 10 KCl, 10 HEPES, 10 $MgCl_2$, 0.4 NaGTP and 2 NaATP (pH 7.3; 280–285 mOsm). HEK 293 culture media was composed of minimal essential media (MEM; 12 360; Invitrogen, Life Technologies/Invitrogen) plus 2% penicillin/streptomycin (15140; Invitrogen, Invitrogen) and 10% fetal bovine serum (16000; Invitrogen, Invitrogen). Cell lysis buffer contained (in mM): 25 Tris (hydroxymethyl) aminomethane (pH 7.5), 150 NaCl, 150 NaF, 0.5 EDTA, and 1.0% Triton X-100 (pH 8.0). Protease and phosphatase inhibitor (PPI) solution was added to the lysis buffer just before use for a final concentration as follows: 1 ug/ml pepstatin A, 1 ug/ml leupeptin, 2 ug/ml aprotinin, 10 ug/ml phenylmethylsulfonyl fluoride, and 1 mM Na_3VO_4. Homogenization buffer contained the following (in mM): 320 sucrose, 10 Tris, 50 KCl, and 1 EDTA (pH 7.8). Wash buffer contained the following (in mM): 25 Tris base (pH 7.5), 150 NaCl, 150 NaF, 0.5 EDTA, and 0.1% Triton X-100. PBS contained the following (in mM): 136.9 NaCl, 2.7 KCl, 10.1 Na_2HPO_4, and 1.8 KH_2PO_4 (pH 7.4). Clozapine N-oxide (CNO; Hello Bio; RRID:SCR_021047) was administered (2.5 mg/kg) in sterile saline (Hospira). Odor A was food odor (General Laboratory Diet 5001; Purina) and Odor B was peppermint odor (Publix Groceries UPC 0-5210007079-7); delivered in mineral oil at 1:100 (Fisher Scientific, 0121-1) and prepared as described previously (Fadool et al., 2004). All salts, sugars, and protease inhibitors were purchased from Sigma-Aldrich or Fisher Scientific. Tissue culture and transfection reagents were purchased from Invitrogen/Gibco.

The following synaptic blockers and channel vestibule blocker were prepared as concentrated stock solutions in aCSF, stored at −20°C until day of use, and then diluted to the following working concentrations: 10 μM gabazine (catalog #104104-50-9, MilliporeSigma), 5 μM NBQX (catalog #ab120045, Abcam), 25 μM (2R)-amino-5-phosphonovaleric acid (AP5; catalog #ab120003, Abcam), 1 nM margatoxin (MgTx; catalog #M8278, MilliporeSigma), 100 μM CNO (Hello Bio), and 100 nM tetrodotoxin (TTX; catalog #120055, Abcam). Before use, MgTx and TTX were additionally mixed with 0.05% bovine serum albumin (BSA fraction V, catalog #BSAV-RO, Sigma-Aldrich) to prevent loss of peptide to tubing and plasticware while recording.

FSU120, a rabbit polyclonal antiserum, was generated against the 46-amino acid sequence 478-MVIEEGGMNHSAFPQTPFKTGNSTATCT TNNNPNDCVNIKKIFTDV-523, representing the unique coding region of the Kv1.3 channel between transmembrane domain 6 and the carboxy terminal. The purified peptide was produced by Genmed Synthesis and the antiserum was produced and then affinity purified by Cocalico Biologicals. This antibody was used for immunoprecipitation (1:1000) and Western blotting detection (1:1500) of Kv1.3 and screened for lack of antigenicity against Kv1.4 and Kv1.5 subfamily members (Vélez et al., 2016). Other antisera used for Western blotting detection were used at the following dilutions and were gifts from investigators or purchased as follows: αKv1.4 (rabbit polyclonal 1:1000; J. O. Dolly, Imperial College, London), αKv1.5 (rabbit polyclonal 1:1000; T. C. Holmes, UC Irvine), αSlack (chicken polyclonal 1:5000; L. Kaczmarek, Yale University), αNa Pan (mouse monoclonal 1:500; catalog #SP-19 Sigma Chemical), and $\alpha\beta$ Tubulin III (rabbit monoclonal 1:3000; catalog #ab52623 Abcam). Donkey anti-rabbit secondary (1:3000; GE Healthcare/GE Healthcare Life Sciences), goat anti-chicken secondary (1:20,000; GE Healthcare), or goat anti-mouse IgG (Fab specific) secondary (1:4000; Sigma Chemical) antisera conjugated to horseradish peroxidase (HRP) were used to visualize proteins via enhanced chemiluminescence (ECL).

cDNA constructs

All Kv1.3 channel coding regions were downstream from a cytomegalovirus promoter. Rat Kv1.3 (rKv1.3) was subcloned into the multiple

cloning region of pcDNA3 (now available only as 3.1; RRID:Addgene_23252; originally 3.0, Invitrogen) at the unique HindIII restriction site as previously described (Holmes et al., 1996). Kv1.3-eGFP was engineered as previously described (Kupper, 1998) to fuse the EGFP reporter to the N terminus of Kv1.3 immediately after the start codon of Kv1.3. Kv1.3-eGFP has been demonstrated to retain the same biophysical properties as that of the wild-type Kv1.3 channel (Spear et al., 2015). Cas9 cDNA was a gift from Feng Zhang (Addgene plasmid #52962; RRID:Addgene_52962). LentiCas9-Blast was inserted into the multiple cloning region of pFUGW using XbaI and BamHI restriction sites (Sanjana et al., 2014).

sgRNA design and CRISPR development

The *Kv1.3* gene is intron-less; therefore, three protospacer adjacent motif or PAM recognition target sites were selected based on their proximity to the 'start' codon and scored using the MIT CRISPR design tool (https://zlab.bio/guide-design-resources) to limit offsite effects. sgRNA oligonucleotide sequences (Bio-Synthesis Inc) were cloned into the BsmBI cloning region of a pLKO.005 vector following the depositor protocol modified for SOC media recovery. The pLKO.005 vector was a gift from Benjamin Ebert (Addgene plasmid #57823; RRID:Addgene_57823). Sequence confirmation was performed by the Florida State University DNA Sequencing Facility. The three sequences targeted were named as follows: sgRNA1- (GCT GCC GCC AGA CAT GAC CG); sgRNA2- (AGA TTG CTG CGG CGA GCG TG); sgRNA3- (AGC ACG TCG GGG GCC CCT TC).

Cell culture

HEK 293 cells were grown in supplemented minimal essential medium (MEM; see Solutions, reagents, and antisera). Before transient transfection, cells were grown to 100% confluency (7 d), dissociated with trypsin-EDTA (Sigma-Aldrich) and mechanical trituration, diluted in MEM to a concentration of 600 cells/ml, and replated on Corning dishes (catalog #25000; Fisher Scientific). cDNA was introduced into HEK 293 cells with a Lipofectamine^{TM} transfection reagent in OptiMEM serum-reduced media (Invitrogen/Gibco) 3–5 d after passage as previously described (Cook and Fadool, 2002). Briefly, cells were transfected for 4 h with 0.75 µg of each cDNA construct per 35-mm dish for electrophysiology. To generate cells for imaging, two 12-mm circle glass coverslips (catalog #12-545-90, Fisher Scientific) were placed flat inside each 35-mm dish before replating. Plasmid DNA with no coding insert (control vector) served as the control to equalize total micrograms of cDNA added to each dish/slip. Cells were used for electrophysiological recordings or microscopic imaging 36–48 h after transfection.

Animals

All mice were housed at the Florida State University (FSU) vivarium on a standard 12 h/12 h light/dark cycle and in accordance with institutional requirements for animal care. Mice were maintained on a reverse light cycle (8 A.M. lights out and 8 P.M. lights on) to facilitate behavioral and metabolic phenotyping for the investigators. Mice were individually housed in conventional-style rodent cages containing separate food and water that could be obtained *ad libitum*. Mice were weaned to either control or moderately high-fat (MHF) diets at postnatal day (P)23 and maintained on that diet for the duration of the experiment (two to six months depending on experiment). Control food (CF) was comprised of 13.5 kcal fat, 59.1% kcal carbohydrate, and 28.05% kcal protein (catalog #5001, Purina Company). MHF diet was comprised of 31.8% kcal fat, 51.4% kcal carbohydrate, and 16.8% kcal protein (catalog #D12266B; Research Diets). The MHF diet was selected to be comparable to a standard American diet (35–40% kcal fat) and significantly higher than that of the control chow (13.5% kcal fat), although the fatty acid profile and sugar content needed for human health differs slightly from rodent diet.

B6;CBA-Tg(Tbx21-cre)1Dlc/J mice with Cre recombinase expression limited to mitral and tufted cells (catalog #024507, The Jackson Laboratory; RRID:IMSR_JAX:024507) were crossed with B6J.129(B6N)-Gt(ROSA)26Sor$^{tm1(CAG-cas9^a,-EGFP)Fezh}$/J mice (catalog #026175, The Jackson Laboratory; RRID:IMSR_JAX:026175) to generate progeny mice with bicistronic spCas9/EGFP expression limited to the mitral and tufted cells. These progeny (referred to as Tbx21-Cre x Cas9/GFP mice) were then injected with virus (see Viral delivery) to introduce sgRNA1 to direct the CRISPR gene-editing. In order to generate Cas9-positive and Cas9-negative littermate controls, heterozygous Tbx21-Cre mice were crossed with homozygous floxed Cas9 reporter mice. This yielded offspring (50%) that lacked Cre recombinase, retained the Lox-STOP-Lox sequence, and prevented Cas9 expression regardless of sgRNA1 viral injection. A total of 238 Tbx21-Cre and Tbx21-Cre x Cas9/GFP male and female mice were used in our experiments. 22 animals were used for AAV serotyping, 91 were used for electrophysiology, 114 for behavioral and metabolic profiling, and *post hoc* tissue analysis, 11 were used for DREADDs experiments (electrophysiology and metabolic profiling), and 21 mice expired or were used for surgical practice. The sequence of experimental events is diagrammed in Figure 1 for ease of reference.

Vertebrate animal protocol and anesthesia

All animal procedures were reviewed and approved by FSU Laboratory Animal Resources (Protocol 202000045) that abided by the American Veterinary Medical Association (AVMA) and the National Institutes of Health (NIH). In preparation for histology, mice were anesthetized by intraperitoneal injection of ketamine (100 mg/kg; Henry Schein Medical Animal Health) and xylazine (10 mg/kg; Akorn Animal Health). This dose of anesthesia was approved as nonsurvival. The level of anesthesia before perfusion was secondarily confirmed by toe pinch and absence of an ocular reflex. In preparation for OB slice electrophysiology, mice were anesthetized with isoflurane (Aerrane; Baxter) using the IACUC-approved drop method and then were killed by decapitation (AVMA Guidelines on Euthanasia, June 2007). In preparation for intracranial surgery, mice were anesthetized in an induction chamber primed with isoflurane (Aerrane) and were maintained under anesthetic state (2% isoflurane gas mixed with oxygen; 0.5 l/min). The analgesic buprenorphine (PAR Pharmaceuticals) was administered immediately following surgery and at 12-h intervals for 1 d following surgery (0.05 mg/kg).

Viral delivery

AAV serotyping optimization

To determine the optimal adeno-associated virus (AAV) for delivery of our sgRNA, we screened five different serotypes for effective transduction of the mitral cell layer (MCL). Viral particles of the form AAV2/xhSynEGFP (x = 2,5,6,8,9) were generated by the University of Iowa Viral Vector Core (titers $> 4.0 \times 10^{12}$ VG/ml) for this purpose. Additionally, we also used a retrovirus of the form AAV2 that was a gift from Jeremy McIntyre (University of Florida) as designed by Matt Wachowiak (Rothermel et al., 2013). The viral particles were intracranially injected into P40 C57BL/6J mice of both sexes ($n = 22$) under stereotaxically-guided surgery [Quintessential Stereotaxic Injector (QSI); Stoelting Company] with coordinates for the MCL (AP +0.45 mm, ML ±0.075 mm relative to the bregma, DV −0.225 mm relative to the cranial surface). Injection volumes (600 Series syringe, Hamilton) were 0.75 or 1.5 µl per hemisphere and injection was performed at a rate of 0.1 µl/min. The retrovirus particles were similarly injected by intracranial delivery but were targeted with coordinates for the aPC and pPC (aPC: AP −0.34 mm, ML +3.0 mm relative to the bregma, DV −4.125 mm relative to the cranial surface; pPC: AP −2.34 mm, ML +1.5 mm relative to the bregma, DV −3.125 mm relative to the cranial surface). At six weeks after injection, mice were terminated by cardiac perfusion and fixed using 4% paraformaldehyde as previously described (Thiebaud et al., 2014). The mice were decapitated, and skulls decalcified to flash-freeze the brain in protective medium (Biju et al., 2008). Coronal sections 14-µm thick (Model 1850UV, Leica Biosystems) were labeled with DAPI nuclear stain (Biju et al., 2008), and stored at −20°C until imaged.

Retro-orbital (RO) sgRNA1 delivery

sgRNA1 was packaged into AAV9 viral particles (~3E+12 VG/ml) using a U6 promotor design (AAV9-hSyn-mCherry-U6-sgRNA virus particle; SignaGen Laboratories). RO injection of sgRNA1 virus was performed on neonatal Tbx21-Cre x Cas9/GFP mice at age P5. Mice were administered a total volume of 100 µl (4×10^{11} VG/mouse) as described by Foust (2009), Yardeni (2011), and Zhang et al. (2011). Briefly, after removing the dam from the home cage, the pups were taken to a

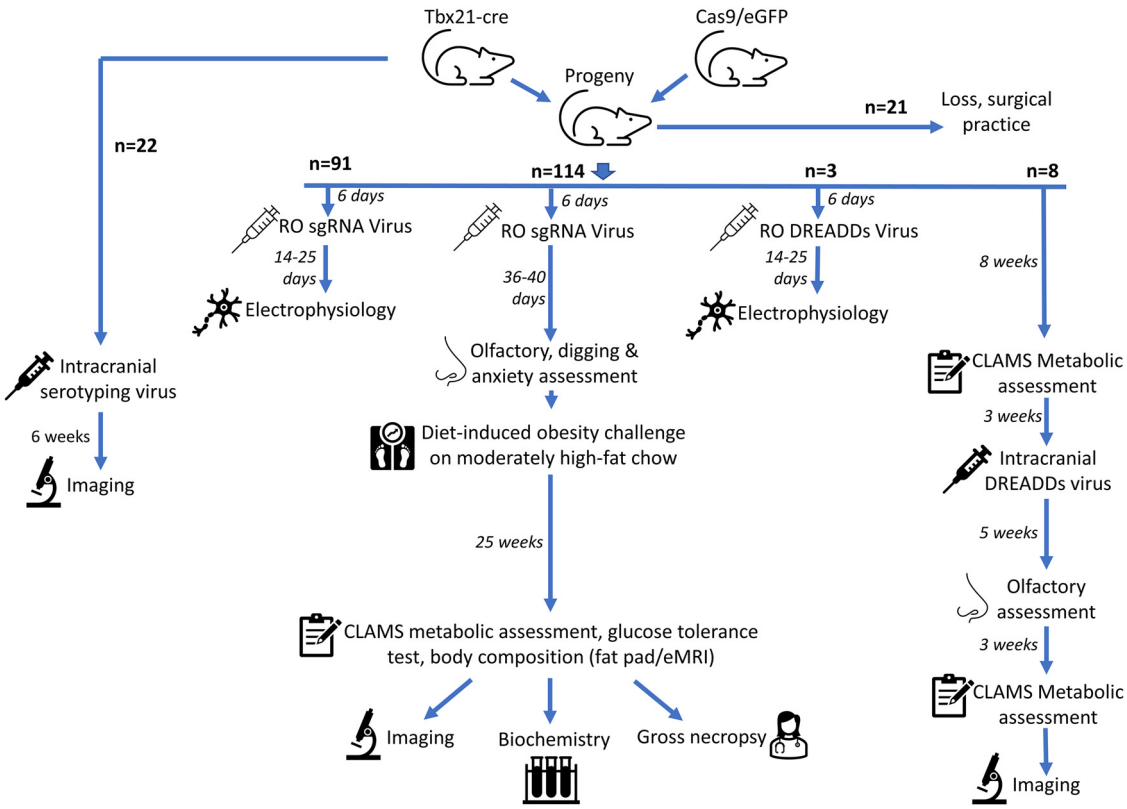

Figure 1. Experimental flowchart for the usage of Tbx21-Cre and Cas9/GFP (Rosa26-flox-Cas9/GFP) mice, and their progeny. Left, A cohort of 22 Tbx21-Cre mice were used for an AAV serotyping assay. Center, Left, 91 Tbx21-Cre x Cas9/GFP progeny mice received CRISPR sgRNA for electrophysiology experiments. RO = retro-orbital. Center, A total of 114 Tbx21-Cre x Cas9/GFP progeny mice received CRISPR sgRNA and were designated for metabolic and biochemical assessment. Many of the mice in this cohort underwent several of the experiments designated in this timeline. Center, Right, 3 Tbx21-Cre x Cas9/GFP progeny mice received RO injection of DREADDs virus for electrophysiology experiments. Right, Eight Tbx21-Cre x Cas9/GFP mice were designated for metabolic and olfactory assessment after receiving intracranial administration of DREADDs virus. All mice within this cohort underwent every experiment. The summary statistics for all experimental analyses can be found in Extended Data Figure 1-1.

dedicated surgical suite isolated from sound. While restraining the pup, a 31-gauge insulin syringe (catalog #831565, Easy Touch) was inserted at a 45° angle to the medial canthus with the bevel facing away from the eye. After advancing the needle ~5 mm, the angle was reduced to 30° and the needle advanced to the RO sinus. The injectate was slowly administered by hand and the pup monitored for excretion of the injectate from the nose (signifying penetration of the nasal cavity). After injection, the pup was placed on a heating pad and rubbed in home cage bedding while recovering for a period of 10 min.

Delivery of DREADDS virus and CNO stimulation

Viral particles of the form AAV9-hSyn-DIO-mCherry-hM4D(Gi) (2.2×10^{13} VG/ml, Addgene) were either intracranially injected for metabolic/behavior profiling or retro-orbitally administered for electrophysiological recording. pAAV-hSyn-DIO-hM4D(Gi)-mCherry was a gift from Bryan Roth (Addgene viral prep #44362-AAV9; RRID:Addgene_44 362). For metabolic profiling, male Tbx21-Cre x Cas9/GFP mice ($n = 8$) underwent stereotaxically-guided surgery at age P74 as described above using 0.5-µl volume at a rate of 0.1 µl/min. The DREADD activating ligand, CNO, is metabolized to clozapine. At high doses, clozapine can have a neurologic effect independent of DREADDS (Manvich et al., 2018). Therefore, for our metabolic and behavior experiments in which mice would be stimulated *in vivo* with CNO, we profiled cohorts ofTbx21-Cre x Cas9/GFP mice twice. We first profiled the mice before being administered viral DREADDs to test the effect of the ligand alone. We then profiled the mice a second time after recovery from the stereotaxic surgery. Mice were allowed to recover for 35 d before being reassessed for metabolic or olfactory phenotype. For electrophysiological recordings, Tbx21-Cre x Cas9/GFP mice at age P5 underwent RO administration as described above. Mice were allowed to recover for 14 d before being killed and prepared for brain slice electrophysiology during which *ex vivo* slices would be stimulated with CNO (see Electrophysiology).

Microscopy and image analysis

HEK cell imaging

Transfected HEK 293 cells were fixed 48-h after transfection in ethanol fixative (Sainte-Marie), and cover slips were then fluoromounted to glass slides for imaging (Fadool and Levitan, 1998). Cells were viewed at 10× magnification and 2600 × 2600 pixel images were captured using a Zeiss Axiovert S100 outfitted with a Xenon lamp and Zeiss Axiocam digital camera and associated AxioVision software (version 4.8, Carl Zeiss Microimaging, RRID:SCR_002677). A set of filter cubes (Carl Zeiss Microimaging) were used to detect EGFP (450- to 490-nm excitation/500- to 550-nm emission) and tagRFP (542- to 582-nm excitation/604- to 644-nm emission). *Post hoc* analysis was performed using Photoshop CS6 (Adobe; RRID:SCR_014199). Only cells containing both an EGFP and tagRFP reporter were assessed and compared with control cells. Cells were categorized as having either unaltered trafficking of Kv1.3 (EGFP expression at the outer boundaries of the cell) or as having altered trafficking of Kv1.3 (tagRFP expression at the outer boundaries of the cell, EGFP expression localized to a center area). The total number of unaltered and altered cells was directly counted for each sgRNA condition.

OB imaging (serotyping)

OB sections were viewed at 40× magnification and images were captured using a Zeiss Axiovert S100 with a Zeiss Axiocam digital camera and associated AxioVision software (version 4.8, Carl Zeiss Microimaging, RRID:SCR_002677). S100 filter cubes (Carl Zeiss Microimaging) were used to detect EGFP (450- to 490-nm excitation/500- to 550-nm emission) and mCherry (540- to 590-nm excitation/590- to 650-nm emission). For the

AAV serotyping assays 2–5 mice per serotype were compared for ability to transduce cells within the MCL. The region of highest fluorescence was imaged for each section. Greater than 30 sections per serotype were imaged in tandem for EGFP, DAPI nuclear stain, and brightfield image. The ability of each serotype to transduce cells within the MCL was visually assessed and compared for the ability to transduce at least one-fifth of MCs within a field of view.

OB imaging (AAV9 transduction efficiency)

OB sections were viewed at 63× magnification and images were captured using a Zeiss LSM 880 confocal microscope outfitted with multichannel QUASAR detector (Carl Zeiss; RRID:SCR_020925). Laser lines were used to detect EGFP (488 nm) and mCherry (594 nm). Image stacks were collected at 0.6 µm. For the determination of transduction efficiency assays, every sixth section was imaged across three mice to avoid redundant imaging of cells that were bisected during sectioning. A total of 77 sections were imaged for MCs, and 89 for TCs. For each sampled section, a similar-sized region of interest (ROI) in the mitral cell or tufted cell layer was scored to compare Cas9 singly labeled cells (EGFP) versus Cas9 + sgRNA1 (EGFP + mCherry) co-labeled cells. ROIs were selected as the area within the dorsal-lateral region with the highest density of target cells. *Post hoc* assessment was performed using Photoshop CS6 (Adobe; RRID:SCR_014199). The number of MCs or TCs within each ROI was determined using the previously described transgenic reporters or confirmed by examining cell morphology as previously characterized (Fadool et al., 2011). The number of double-labeled target cells expressing a viral reporter was then counted for each image and a proportion totaled for each mouse. A total of 870 MCs and 639 TCs were categorized in this manner.

Biochemistry

OB membranes were either purified by centrifugation or Kv1.3 protein was immunoprecipated as previously (Fadool and Levitan, 1998; Murphy et al., 2001; Cook and Fadool, 2002; Fadool et al., 2004; Marks and Fadool, 2007; Vélez et al., 2016). Briefly, to prepare membranes by centrifugation, OB tissues were homogenized for 50 strokes using a Kontes tissue grinder (size 20) in ice cold HB solution containing protease inhibitors. Homogenized tissue was centrifuged twice at ~2400 × *g* (3800 RPM) for 30 min at 4°C in an Eppendorf centrifuge (model 5416, Eppendorf) to remove cellular debris. The supernatant was centrifuged in a Beckman ultracentrifuge (model L8-M; Beckman; RRID: SCR_019674) at 110,000 × *g* (40,000 RPM) for 2.5 h at 4°C. The resulting pellet was resuspended in HB solution and tip sonicated on ice three times for 20 s each with a Tekmar sonicator (setting 50; Tekmar). For immunoprecipitation of Kv1.3 protein, OBs were individually homogenized using ice-cold lysis buffer containing PPIs as in Fadool et al. (2000). Homogenates were orbitally rotated for 30 min at 4°C, then clarified by centrifugation at 14,000 × *g* (Eppendorf) for 30 min at 4°C. Collected supernatants were precleared for 3 h with 3 mg/ml protein A-Sepharose (catalog #17-0780-01, Citiva Company, previously GE Healthcare). Kv1.3 proteins were immunoprecipitated from the cleared lysates using anti-FSU120 (see Solutions/reagents, and antisera) in an overnight incubation with 2–4 µg/µl of antibody at 4°C. The immunoprecipitates were washed four times with wash buffer and stored at −20°C until separated by SDS-PAGE as previously performed (Tucker and Fadool, 2002).

For SDS-PAGE followed by Western analysis, nitrocellulose membranes (catalog #162-0115, 0.45 µM, Bio-Rad) were blocked with 5% nonfat milk (catalog #170-6404, Bio-Rad). Nitrocellulose was incubated overnight at 4°C with primary antisera and then membranes were incubated with species-specific HRP-conjugated secondary antisera for 90 min at room temperature (rt). Labeled proteins were visualized by ECL (catalog #RPN2106, Citiva Company) and band pixel density was quantified using scanning densitometry normalized to β Tubulin III [ImageJ (as Fiji), NIH; RRID:SCR_002285] as previously described (Fadool and Levitan, 1998; Cook and Fadool, 2002; Marks and Fadool, 2007; Vélez et al., 2016).

Electrophysiology

Heterologous expression in HEK 293 cells

Hoffman modulation contrast optics were used to visualize HEK 293 cells at 40× magnification (Axiovert 135, Carl Zeiss). Patch electrodes were fabricated from Sutter borosilicate glass (BF150-86-15; Sutter Instruments) with pipette resistances between 9 and 14 MΩ as fabricated with a vertical puller (PP-830; Narishige) and fire polished to ~1 µm with a microforge (MF-830; Narishge). Macroscopic Kv1.3 currents were recorded at rt from cell-attached membrane patches of HEK 293 cells using an Axopatch-200B (Molecular Devices/Molecular Devices, RRID:SCR_011323) patch-clamp amplifier. The cell-attached configuration was achieved after carefully contacting the cell surface with the tip of the patch pipette and applying a gentle suction to create a very high resistance (>1 GΩ) seal. Both the seal and pipette capacitance were electronically compensated before recording. All voltage signals were generated and data were acquired with the use of an Axon Digidata 1200 board with pClamp v11 software (Molecular Devices/Molecular Devices; SCR_011323). Recordings were filtered at 2 kHz and digitized at 2–5 kHz. Patches were routinely held at a holding potential (V_h) of −90 mV and stepped in 10- to 20-mV depolarizing potentials to +40 mV (V_c) using a pulse duration (P_d) varying from 100 to 1000 ms. Longer P_d were generally delivered at intervals of 60 s or longer to prevent cumulative inactivation of the Kv1.3 channel (Marom et al., 1993). Peak transient current was defined as the greatest current observed after voltage activation.

OB slice recordings

OB slices for electrophysiological recordings were acquired from Tbx21-Cre x Cas9/GFP mice between the ages P19-P35 as described previously (Fadool et al., 2011). In conjunction with the timing of our RO delivery of sgRNA1, all mice had ≥14 d of viral expression and hence potential for CRISPR genome editing of Kv1.3 channel before recording. To prepare for recording, mice were anesthetized by inhalation of isoflurane, quickly decapitated, and the OBs were rapidly exposed by removing the dorsal and lateral portions of the skull (Nickell et al., 1996). The OBs (while still attached to the forebrain) were quickly removed, glued to a sectioning block with Superglue (Lowe's Home Improvement) and submerged in oxygenated (95% O_2/5% CO_2), ice-cold, sucrose-modified aCSF to prepare the tissue for sectioning. Coronal sections (300 µm) were cut in oxygenated, ice-cold, sucrose-modified aCSF using a Series 1000 Vibratome (Leica; RRID:SCR_016495). The OB sections were allowed to recover in an interface chamber (Krimer and Goldman-Rakic, 1997) with oxygenated, sucrose-modified aCSF at 33°C for 15 min and then were maintained at rt in oxygenated normal aCSF until needed (Fadool et al., 2011). OB slices were recorded in a continuously-perfused (Ismatec; 1–2 ml/min), submerged-slice recording chamber (RC-26, Warner Instruments) with aCSF at rt.

OB slices were visualized at 10× and 40× using an Axioskop 2FS Plus Microscope (Carl Zeiss Microimaging) equipped with fluorescent excitation and infrared detection capabilities (CCD100; Dage-MTI). Electrodes were fabricated from borosilicate glass (#1405002; Hilgenberg GmbH) to a diameter of ~2 µm to yield pipette resistances ranging from 6 to 12 MΩ. Positive pressure was retained when navigating through the OB laminae until a high resistance seal (1.5–10 GΩ) was obtained on a positionally-identified MC in the slice (Fadool et al., 2011). The morphology and biophysical properties of the neurons were used to distinguish MCs from TCs (Nickell et al., 1996; Schoppa and Westbrook, 2001; Fadool et al., 2004; Fadool and Kolling, 2020). In addition, Tbx21-Cre x Cas9/GFP mice injected with AAV9-sgRNA1 or AAV9-hM4D (Gi) provided green and red fluorescent markers, respectively, that served as secondary confirmation of cell identity and were readily distinguishable. The cell-attached configuration was established by applying gentle suction to the lumen of the pipette while monitoring resistance. Whole-cell access was obtained by applying a 100 ms, 1-mV pulse across the membrane while applying sharp suction to the lumen of the pipette. Membrane voltage and current properties were generated using pCLAMP, version 9 or 10, in conjunction with a Multiclamp 700B amplifier (Molecular Devices; RRID:SCR_011323/Molecular Devices; RRID:SCR_018455). The analog signal was filtered

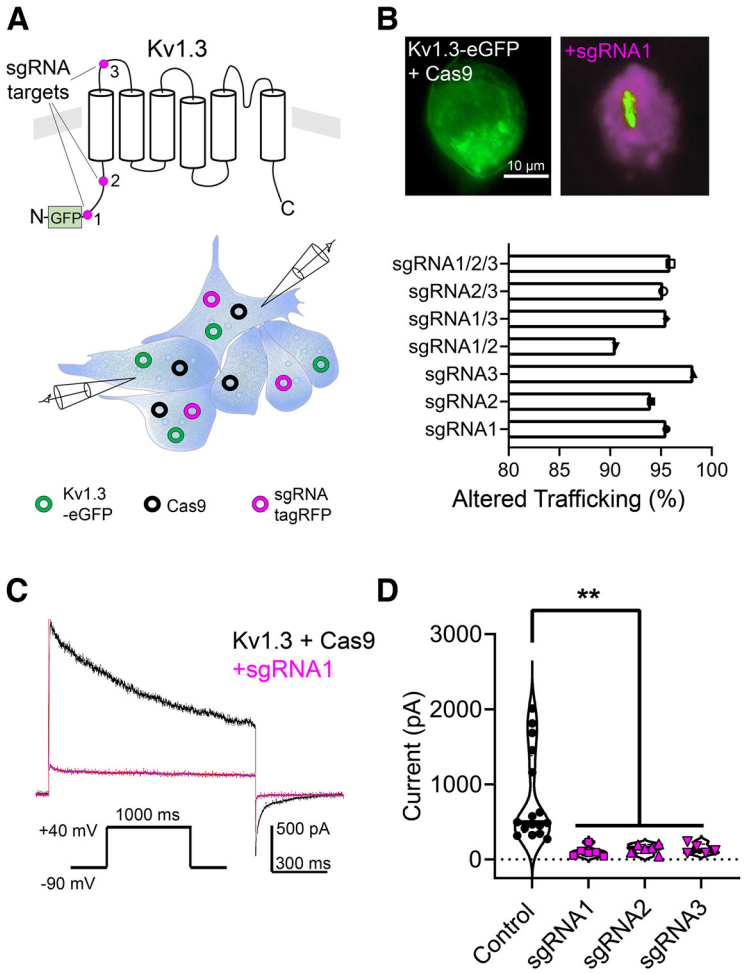

Figure 2. *In vitro* assessment of CRISPR sgRNA. ***A***, Top, Cartoon diagram of the secondary structure of a Kv1.3 monomer with representative target sites of three engineered sgRNA at PAM recognition sequences. Bottom, *In vitro* experimental paradigm demonstrating the various plasmids used in HEK 293 cells. ***B***, Top, Left, Representative photomicrograph of a HEK 293 cell transfected with Kv1.3-eGFP + Cas9 cDNA. Top, Right, Same, plus sgRNA cDNA. Bottom, Histogram plot of the percentage of HEK 293 cells with altered membrane trafficking in seven separate transfections. Different combinations of sgRNA are aligned on the *y*-axis. sgRNA1 95.54% $n = 1820$, sgrna2 94.02% $n = 1086$, sgrna3 98.2% $n = 2702$, sgrna1/2 90.56% $n = 1903$, sgrna1/3 94.54% $n = 1681$, sgrna2/3 95.22% $n = 2307$, sgrna1/2/3 95.93% $n = 2580$. ***C***, Representative voltage-clamp recordings acquired from HEK 293 cells transfected with the two conditions shown in ***B***, Top. $V_h = -90$ mV, cells stepped to $V_c = +40$ mV with $P_d = 1000$ ms and IPI of 45 s. ***D***, Violin plot of the peak current amplitude of a population of cells recorded as in ***C***, substituting the three different sgRNA mapped as in ***A*** (one-way ANOVA, $F_{(3,29)} = 6.679$, $^{**}p = 0.0014$). In this and subsequent violin blots, the median is shown as a solid line and the dashed lines represent the upper and lower quartiles.

at 2 kHz and minimally digitally sampled every 100 µs with a Digidata 1440A digitizer (Molecular Devices, Molecular Devices; RRID:SCR_021038). The pipette capacitance was electrically compensated through the capacitance neutralization circuit of the Multiclamp 700B amplifier. Resting membrane potentials (RMPs) were corrected for a calculated −7-mV junction potential offset. Membrane capacitance and input resistance were acquired from the membrane test function of Clampex 10.7 (Molecular Devices).

After establishing a whole-cell configuration, cells were first sampled for adequate resting potential (less than −55 mV) and proper access resistance (<40 MΩ) before initiating either a series of current- or voltage-clamp recordings. For current-clamp recordings, perithreshold current levels were determined by incrementally injecting 1000-ms-long, 25-pA steps of current every 10 s, starting at −50 pA. Following the determination of spike threshold, cells were stimulated with 10 super-threshold sweeps of 5000-ms duration (typically ranging from 25 to 250 pA) every 30 s to acquire spike frequency and latency data.

Spike amplitude, time to peak, anti-peak amplitude, latency to first spike, spike event frequency, interburst interval, intraburst interval, and burst length were measured as described previously (Balu et al., 2004; Fadool et al., 2011; Mast and Fadool, 2012). A burst was defined as three or more consecutive spikes within a period of 100 ms or less as established by Balu et al. (2004). MC firing is intrinsically intermittent and is characterized by variable burst characteristics. As such, classical means of computing spike timing variability, such as peristimulus time histograms, were less suitable for the behavior of these neurons. Therefore, alternative means of spike analysis were applied as described previously (Balu et al., 2004). For voltage-clamp recordings, cells were typically held at a $V_m = -80$ mV and then stepped from −100 mV to a family of V_c in +20-mV increments using a $P_d = 400$ ms and stimulation interval of 45 s. Evoked currents were acquired in the presence of synaptic blockers (see Solutions, reagents, and antisera), and when needed, the addition of 20 µM TTX to eliminate unwanted AP spiking.

Olfactory behavior

An odor habituation-dishabituation paradigm was performed (Fadool et al., 2004; Tucker et al., 2008; Al Koborssy et al., 2019) to determine changes in odor discrimination for mice administered sgRNA1 for CRISPR genome editing or DREADDs as described above. For a subset of mice administered sgRNA1 for CRISPR genome editing, two tests for anxiety-like behavior were additionally performed [light-dark box (LDB); marble burying assay] and also a gross test for general anosmia (hide the cookie assay) to determine movement and digging behavior according to our previous works (Tucker et al., 2012b; Huang et al., 2018). The only exception was that mice were not removed to a home cage following acclimation, and before presentation of marbles or objects, so as to reduce total handling of animals. For the behavioral experiments where mice received sgRNA1, viral particles were administered to Tbx21-Cre x Cas9/GFP mice by RO delivery at P5. Mice were then behaviorally tested between P35-P40, which allowed a minimum of one month of viral expression before behavioral assay. For mice administered DREADDs virus, Tbx21-Cre x Cas9/GFP mice intracranially received DREADDs virus at P74–P75 and were then tested 35–42 d after surgery. Here, mice performed the behavioral assay twice, one week apart, using a counter-balanced design of PBS versus CNO, each of which were intraperitoneally delivered 45 min before behavioral testing. In the habituation/dishabituation odor discrimination assay, mice were habituated to repeated presentation of an odor ("Odor A"), and then once habituated to that stimulus, they were presented a novel odorant ("Odor B") and dishabituation was scored. The change in exploratory time between the dishabituation/habituation is defined as the discrimination ratio. Briefly, mice were tested ~2 h into the dark phase in an isolated room protected from sound. Mice were removed from their home cage and introduced to the testing chamber (18.75 cm wide × 30 cm long, × 12.5 cm high) that contained standard depth β chip bedding without access to food or water. The "Odor A" was diluted 1:100 by volume in mineral oil, applied to a cotton swab, and then presented to the mouse through the top of the testing cage. The time of active investigation/smelling of the odor was recorded over a 1 min trial period. Active investigation was defined as oriented to the cotton swab within 1 cm of the tip with sniffing. This was repeated every 60 s for 7 trials to produce a decreasing

investigation time (habituation). On the eighth trial, "Odor B" (novel odor) was similarly diluted, presented, and time of exploration was scored (dishabituation). For our behavioral assays, the investigator was blinded to the treatment condition.

Metabolic assessments

Mice were metabolically profiled using indirect calorimetry. Mice were housed in Comprehensive Laboratory Animal Monitoring System (CLAMS) cages (Columbus Instruments; RRID:SCR_016718) to determine oxygen consumption (VO_2; ml/kg/min), respiratory exchange ratio (RER; VO_2/VCO_2), EE (kcal/h; Lusk and Bois, 1924), locomotor activity, and ingestive behavior (caloric and water consumption) as previously performed (Bell and Fadool, 2017; Fadool and Kolling, 2020; Chelette et al., 2022). Mice had *ad libitum* access to food and water in overhead feeders attached to electronic balances that could detect both disturbance and decrease in mass. EE was calculated according to the Lusk equation $(3.815 + 1.232 \times \text{RER}) \times VO_2$. Locomotor activity was continuously recorded using optical beams along the *x*-axis of the cage so that consecutive photograph beam breaks could be scored as ambulatory movement. All data were recorded in intervals using Oxymax software (CLAX; Columbus Instruments; RRID:SCR_016718) and each interval measurement represented the average value during a 30-s sampling period per cage. In total, mice were housed in the CLAMS for 6 d. No data were acquired in the CLAMS during the first 3 d in the chambers to permit acclimation to the environment, and then experimental data were computed for each light/dark phase over 3 d (Williams et al., 2002; Fadool et al., 2004; Tucker et al., 2008; Bell and Fadool, 2017). Time 0 reported for the CLAMS analyses represented the start of the dark or the light cycle, respectively. Data were graphed in a normalized fashion to visually compare the response of either genotype or CNO treatment, respectively, across mouse subjects for a particular metabolic variable, and non-normalized data were used in an unpaired- or paired-subject analysis (repeated measure; RM) as described in the statistical analyses below.

To monitor serum glucose clearance in response to a bolus of glucose, intraperitoneal glucose tolerance tests (IPGTTs) were performed after a 6-h fast starting from the beginning of the dark phase (Chelette et al., 2019). After initial determination of fasting blood glucose, 2 g glucose per kilogram of bodyweight was administered by intraperitoneal injection from a 25% glucose solution (University of Virginia Vivarium Protocols, Susanna R. Keller). Glucose levels were measured from collected tail blood samples taken at 15 m, 30 m, 60 m, 90 m, 2 h using an Ascensia Contour Blood Glucose Monitoring System (Ascensia Diabetes Care US). Integrated area under the curve (iAUC) was computed to determine clearance as previously (Marks et al., 2009). Serum and organ chemistry measurements for total cholesterol, triglycerides, and leptin were performed by the University of California Davis at the National Mouse Metabolic Phenotyping Center using institutional protocols.

Body composition analysis

Body composition was assessed *in vivo* using an EchoMRI machine (EchoMRI LLC; RRID:SCR_017104) and manufacturer software. After calibration of the machine, mice were gently restrained within a 2" diameter sample tube. The sample tube was inserted into the EchoMRI, and mice were assessed for fat mass, lean mass, total water, and free water. Body fat percentage was calculated as:

$$bf\% = \frac{fatmass(g)}{\text{lean mass (g)} - freewater(g)} \times 100\%$$ (Chelette et al., 2022).

Following body composition and metabolic assessment, mice were killed and their fat pads were excised and weighed by an investigator who was blinded to the condition. Interscapular brown, mesenteric, retroperitoneal,

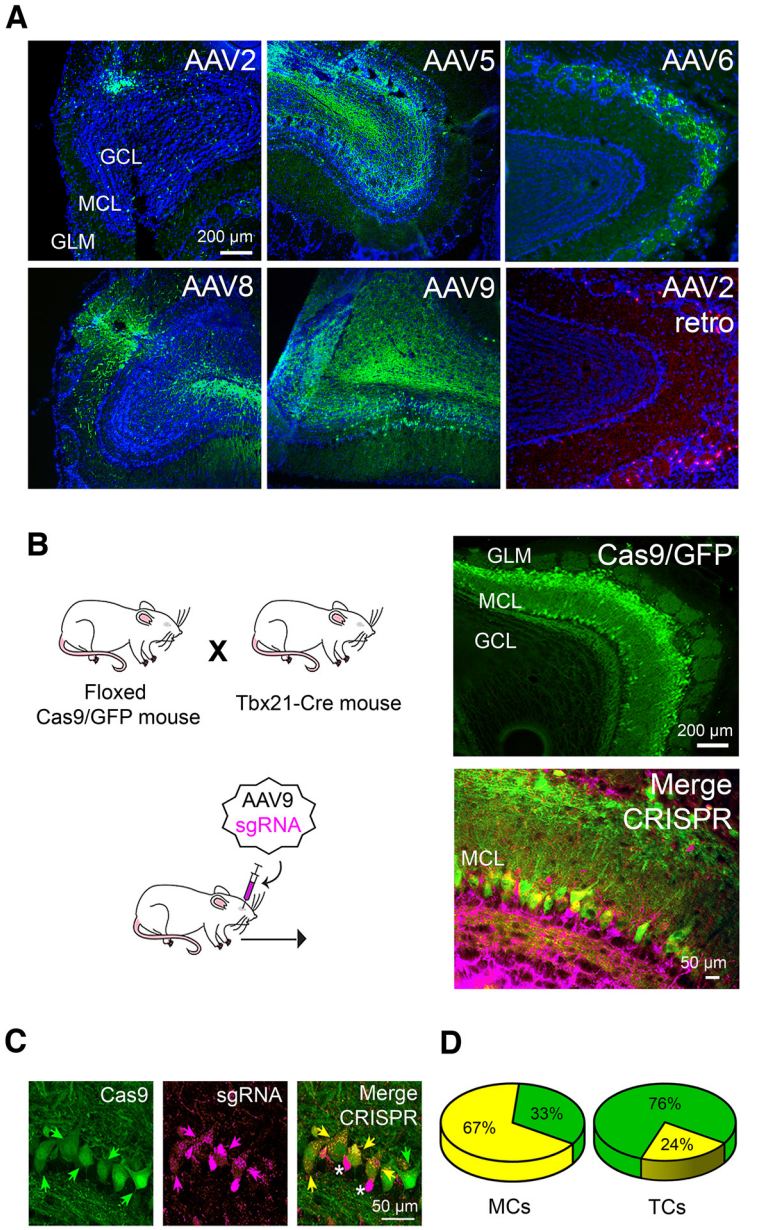

Figure 3. *In vivo* delivery of CRISPR-Cas9 to mitral and tufted cells. ***A***, Photomicrographs of coronal sections of the OB following intracranial transduction of AAV2, 5, 6, 8, or 9 engineered with a GFP reporter or AAV2/retro with an RFP reporter. GCL = granule cell layer, MCL = mitral cell layer, GLM = glomerular cell layer. ***B***, Left, Schematic of breeding design; B6;CBA-Tg(Tbx21-cre)1Dlc/J mice (Tbx21-Cre mouse) were bred with hemizygous B6J.129(B6N)-Gt(ROSA)26Sor$^{tm1(CAG-cas9^a,-EGFP)Fezh}$/J mice (Floxed Cas9/GFP mouse) to generate Tbx21-Cre x Cas9/GFP progeny that were retro-orbitally (RO) transduced with AAV9-mCherry-sgRNA1. Right, Top, Photomicrograph of OB neurolaminae from Tbx21-Cre x Cas9/GFP progeny demonstrating Cas9/GFP expression limited to the M/TCs. Right, Bottom, Same, but after RO transduction of AAV9-sgRNA1 (CRISPR). Note that the sgRNA transduces neurons across all neurolaminae, delivering full CRISPR-Cas9 to the M/TCs (Merge CRISPR). ***C***, Photomicrographs of confocal images acquired in the MCL at high magnification with excitation for Cas9/GFP (Cas9), AAV9-mCherry-sgRNA (sgRNA), and then merge (Merge CRISPR). Arrows = double labeling, * = non-MCs without Cas9. ***D***, Pie chart summary of 166 microscopic sections as in ***C*** that were acquired from three mice to determine the percentage of double labeling for both Cas9/sgRNA and capable of CRISPR gene editing in mitral (MCs) versus tufted (TCs) cells. Further assessment of Cas9/GFP expression in the OB versus the versus the SCN of the hypothalamus in Tbx21-Cre x Cas9/GFP progeny mice can be found in Figure 4.

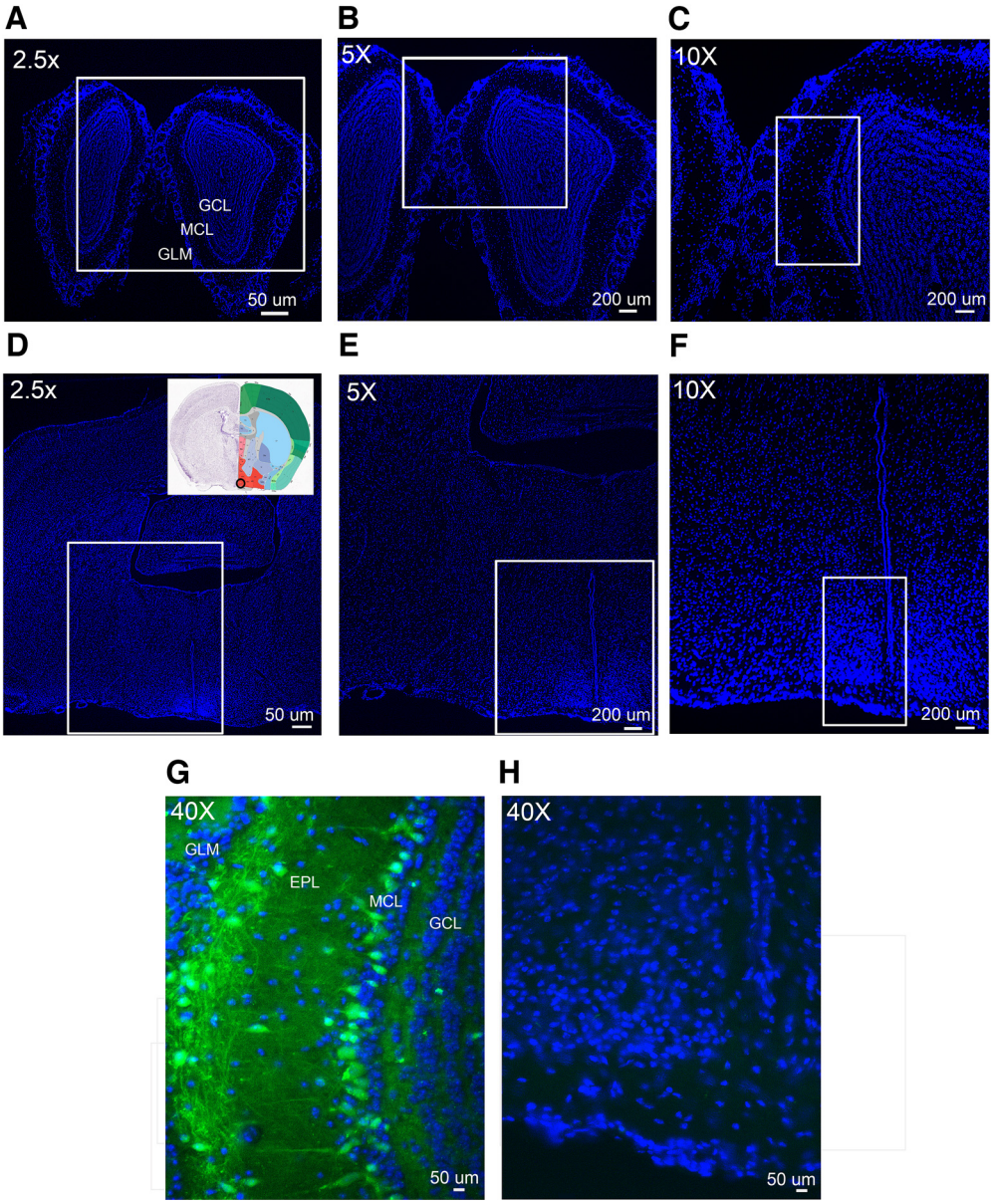

Figure 4. Assessment of Cas9/GFP expression in the OB versus the SCN of the hypothalamus in Tbx21-Cre x Cas9/GFP progeny mice. ***A–C*** (2.5–10×), Photomicrographs of coronal sections of the OB labeled with DAPI nuclear stain to highlight neurolaminae. The overlayed box corresponds to the location of the succeeding image. GCL = granule cell layer, MCL = mitral cell layer, GLM = glomerular layer. ***D–F*** (2.5–10×), Photomicrographs of coronal sections of the hypothalamus similarly prepared as in ***A–C***. ***D***, Inset, Image from the Allen Brain Atlas with a subcortical map overlayed on neurolaminar landmarks. The circled region corresponds to the SCN of the hypothalamus. ***G***, ***H*** (40×), Higher power photomicrographs of the region of interest from ***C***, ***F***, respectively. Cas9/GFP (green channel, 488-nm excitation) is merged with DAPI nuclear stain where both regions are matched for exposure time. Note expression of Cas9/GFP in M/TCs of the OB in ***G*** and an absence of Cas9/GFP-labeled cell bodies in the SCN of the hypothalamus in ***H***.

and gonadal fat pads as well as livers were weighed separately (Tucker et al., 2012a; Chelette et al., 2019).

Experimental design and statistical analyses

The timing ofexperiments and categorized sample sizes can be found within the schematic of Figure 1. For electrophysiological recordings, the reported sample size is the number of cells, for which no more than two cells were acquired from a single mouse. For metabolic profiling, the reported sample size is the number of measurements acquired for a given variable, for which no more than three measurements were acquired for each mouse, and these were acquired across three consecutive days rather than averaged. Specific variables required for independent replication (sample size, number of animals, sexes used, and justification) and full statistical analyses are available in Extended Data Figure 1-1.

Before performing any statistical comparisons, data were first analyzed with the Dixon's Q test to identify any outliers. Then data were checked for normal distribution and homogeneity of variance using the Fmax test. Analysis of data collected did not identify any outliers. Where collected data violated homogeneity of variance (failed the Fmax test), the selection of applied statistics was changed to the nonparametric equivalent. Current amplitude recorded in HEK 293 cells was analyzed using a one-way ANOVA with cDNA construct as the factor at the 95% confidence level ($\alpha < 0.05$). Independent sample population comparisons of MC biophysical properties between Control and CRISPR mice (RMP, threshold I, spike frequency, action potential (AP) time to half-amplitude, AP rise and decay slopes, voltage-clamped baseline current, and percent MgTx suppression) were analyzed using a Student's *t* test or Mann–Whitney *U* at the 95% confidence level ($\alpha < 0.05$). Behavioral measurements of object burying (marble), exploration (habituation/dishabituation), or compartment moving (LDB transitions) were analyzed using a Student's *t* test or Mann–Whitney *U*, or by applying a mixed two-way RM ANOVA with object and genotype as factors (hide the cookie) or

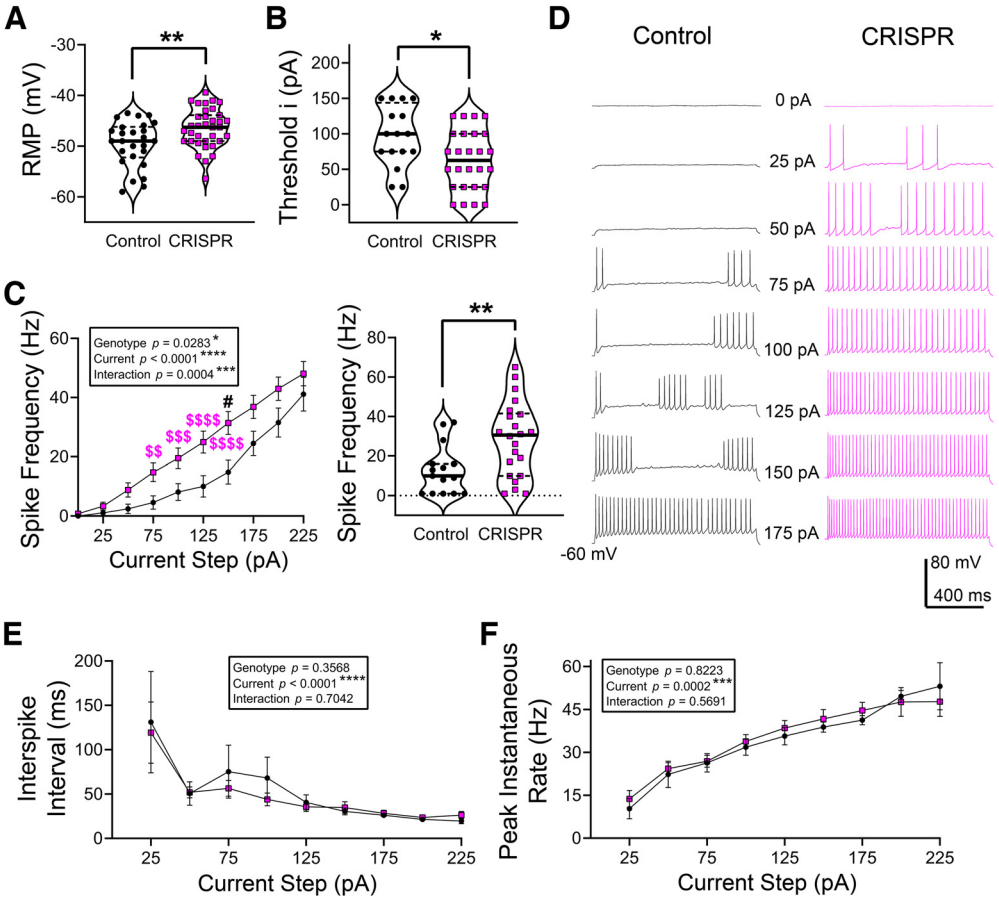

Figure 5. *Ex vivo* assessment of mitral cell increased excitability after CRISPR. ***A***, Violin plot of the RMP acquired from mitral cells (MCs) recorded from brain slices prepared from Control (Cas9(–) with sgRNA1) versus CRISPR (Cas9(+) with sgRNA1) mice. Student's *t* test, $^{**}p = 0.0027$. ***B***, Same as ***A*** but comparing the threshold current (rheobase) required to evoke APs. Mann–Whitney *U*, $^{*}p = 0.0195$. ***C***, Left, Line graph of AP firing frequency versus current magnitude for 37 MCs recorded from Control (●) versus CRISPR (■) mice. Two-way mixed RM ANOVA using genotype and current as factors. See box for ANOVA results in this and subsequent figures. Sidak's *post hoc* test $\#p = 0.0497$ at 150 pA, main effect of genotype; $\$\$p < 0.01$, $\$\$\$p < 0.001$, $\$\$\$\$p < 0.0001$, interaction compared with 25-pA step. Right, Violin plot of the AP spike frequency at the 150-pA step from the recorded population of cells at the left. Mann–Whitney *U*, $^{**}p = 0.0090$. ***D***, Representative AP activity for MCs recorded in Control and CRISPR mice. Each MC was stimulated with a series of injected current steps for 1 s that increased in increments of 25 pA from −50 to 175 pA. ***E***, Line graph of ISI versus current magnitude for 41 MCs recorded from Control versus CRISPR mice. Two-way mixed RM ANOVA using genotype and current as factors. ***F***, Same as ***E*** but for PIR.

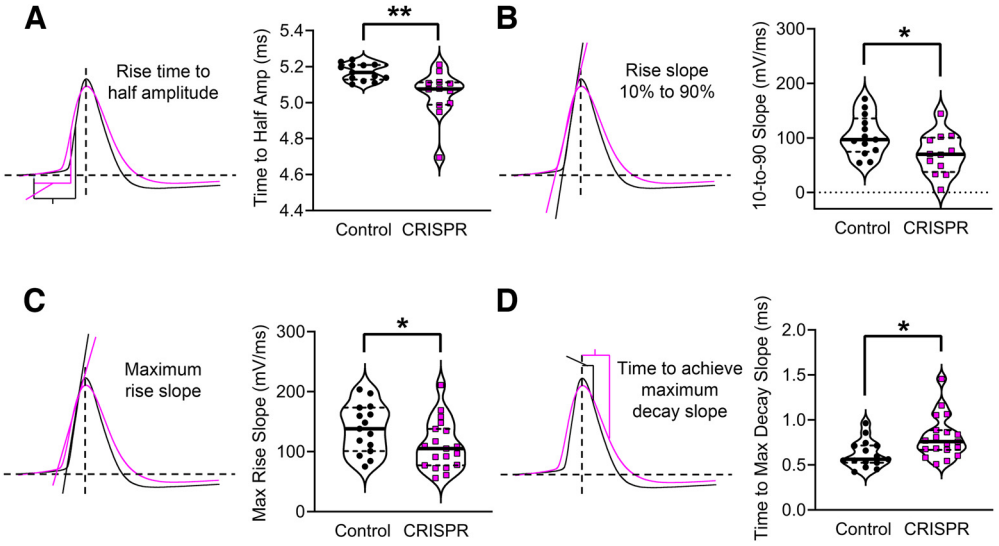

Figure 6. AP shape for MCs recorded in Control versus CRISPR mice. Values for ***A***–***D*** compared at the 150-pA current injection step (follow-up test point of significance from Fig. 4*C*). ***A***, Left, AP diagram of the parameter "Rise time to half amplitude." Black, representative Control AP. Magenta, representative CRISPR AP. Right, Violin plot comparing rise time to half amplitude for APs recorded from a population of Control (●) versus CRISPR (■) mice; *t* test with Welch's correction, $^{**}p = 0.0093$. Same as in ***A*** but for ***B***, "Rise slope 10% to 90%". Mann–Whitney *U*, $^{*}p = 0.0457$. ***C***, "Maximum rise slope." Mann–Whitney *U*, $^{*}p = 0.0396$. ***D***, "Time to achieve maximum decay slope." Student's *t* test, $^{*}p = 0.0125$.

location and genotype as factors (LDB compartment times); at the 95% confidence level ($\alpha < 0.05$). Serum chemistry measurements of blood glucose, total cholesterol, triglycerides, and leptin were analyzed using a Student's *t* test or Mann–Whitney *U* at the 95% confidence level ($\alpha < 0.05$). Metabolic data from the CLAMS (RER, VO_2, and heat expenditure) were analyzed using a mixed two-way RM ANOVA with genotype and time (hours) as factors or with drug treatment (CNO) and time (hours) as factors; each within light or dark phases and at the 95% confidence level ($\alpha < 0.05$). Comparison of these same metabolic data as 12-h means across light versus dark phase within genotype was analyzed using a one-tailed, paired *t* test ($\alpha < 0.05$). The metrics of food intake, meal size, water intake, and locomotor activity were summarized by mean over the 12-h dark or light phase and compared across genotype (Control vs CRISPR) or drug treatment (saline vs CNO) using a Student's *t* test or Mann–Whitney *U* at the 95% confidence level ($\alpha < 0.05$). Body weight over age measurements were analyzed with a mixed two-way RM ANOVA using genotype and time (weeks) as factors. For the ordinary or RM ANOVA tests, the Sidak or Bonferroni method for multiple comparison testing was used as the *post hoc* analysis to make mean-wise comparisons between genotypes or between drug treatments. Males and females were analyzed as separate cohorts. All reported values in the text represent the mean ± SD. Figures largely report individual data points using violin graphs and represent number of mice, number of cells, or number of metabolic measures as noted in the figure legends. Sample sizes for the line graphs are reported in the figure legends. Where means are reported in the figures, the error is reported as the SEM. Individual *p* values are reported for each experiment within the corresponding graph with the individual F statistic described in the results section. Statistical tests were performed using GraphPad Prism 9 (GraphPad Software) while the graphs and figures were produced using a combination of Origin v8 (OriginLab Corporation; RRID:SCR_014212), Adobe Photoshop CS4 (Adobe; RRID:SCR_014199), and GraphPad Prism 9 (GraphPad Software; RRID:SCR_002798).

All electrophysiological data were analyzed using pClamp, version 10 (Clampfit 10.7; Molecular Devices; RRID:SCR_011323) and Igor Pro, version 6.12A (WaveMetrics Inc.; RRID:SCR_000325) with the plug-in NeuroMatic, version 2 (written by Jason Rothman; http://www.neuromatic.thinkrandom.com; RRID:SCR_004186). CLAMS data were outputted using CLAX version 2.2.15 (Columbus Instruments).

Results

Designed sgRNAs suppress Kv1.3 activity and can be targeted effectively to mitral and tufted cells in the OB

We designed three sgRNAs to selectively edit the *Kv1.3* gene in M/TCs. These sgRNAs targeted DNA sequences upstream of spCas9 PAM recognition sites encoding the N-terminal region and first extracellular loop of Kv1.3 (Fig. 2*A*). After cloning these constructs into an appropriate plasmid (pLKO5.sgRNA.EFS.tRFP) with a fluorescent reporter, we examined their ability to decrease Kv1.3 channel expression in a heterologous expression system. Using lipofectamide-based strategies, HEK 293 cells were co-transfected with plasmid cDNA for a Kv1.3-eGFP fusion protein (Spear et al., 2015) plus Cas9, plus or minus one of three sgRNAs (Fig. 2*A*,*B*). Three microscopic fields of view were examined at 40× across three transfection sets for each sgRNA construct to determine altered surface trafficking of the channel as shown in Figure 2*B*. In control transfections, Kv1.3-eGFP is successfully trafficked to the plasma membrane (Fig. 2*B*) because of ER-exit motifs located downstream of the CRISPR target sites (Deutsch, 2002; Spear et al., 2015). Successful CRISPR targeting prevented trafficking of the N-terminal GFP to the cell membrane. Each combination of sgRNA was able to prevent this trafficking in >90% of the total cells examined. Combinations of several sgRNA were not observed to be more effective than individual sgRNA. Consequently, each sgRNA was then investigated separately for its ability to reduce Kv1.3 current

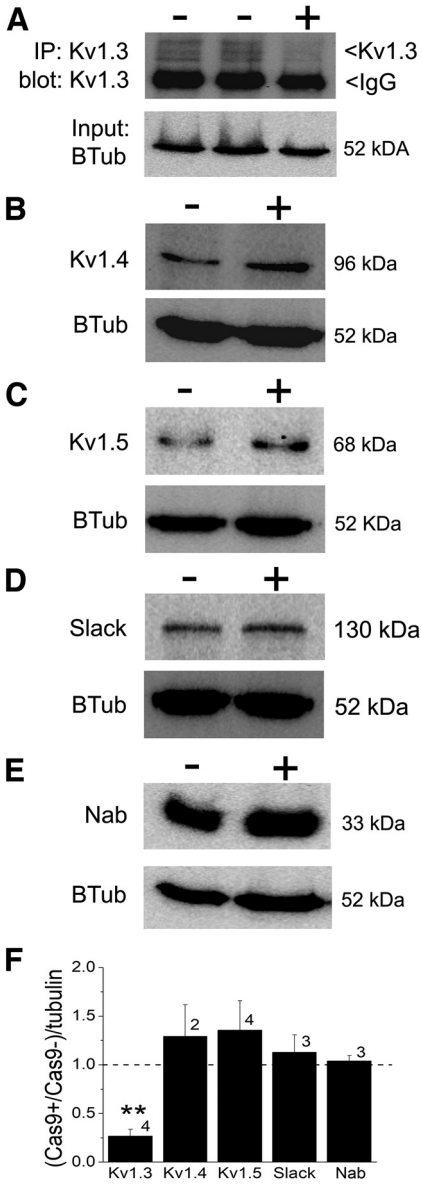

Figure 7. OB expression levels of ion channel protein in Control versus CRISPR mice. ***A***, OB lysates were used to immunoprecipitate (IP) Kv1.3 channel protein using a polyclonal, affinity-purified antisera (FSU120) against the amino terminus of the channel. Immunoprecipitates were separated by 10% SDS-PAGE, electrotransferred to nitrocellulose, and blotted with FSU120 (blot: Kv1.3). Epichemiluminescense was used to visualize the expected Kv1.3 protein (<Kv1.3; $M_w = 58$ kDa). IgG arrow, heavy chain of the immunoglobulin. "–" = Control mice (Cas9 negative) and "+" = CRISPR mice (Cas9 positive). Input was probed with $\alpha\beta$ Tubulin III (BTub) as a loading control. ***B–E***, OB membrane proteins were similarly separated by SDS-PAGE, electrotransferred to nitrocellulose, and blotted with various antisera to compare expression levels in the Control (–) versus CRISPR (+) mice. M_w as noted. Slack = K_{Na} channel, Nab = Na channel β subunit. ***F***, Line densitometry was performed to determine pixel immunodensity ratios normalized to the associated loading standard. Bar graph denoting Cas9(+)/Cas9(–) ratios normalized to BTub for each channel protein. Student's *t* test with arcsine transformation for percentage data, $^{**}p = 0.0022$, sample sizes as noted represent number of membrane preparations. Ratio of 1.0 (dashed line) indicates no difference in expression.

elicited by voltage stimulation using patch-clamp electrophysiology. Transfected HEK 293 cells were held at −90 mV (V_h) and stepped to a depolarizing command potential (V_c = −40 mV; Fig. 2*C*) for 1000 ms pulse duration. Patches co-expressing Kv1.3 + Cas9 elicited macroscopic currents with peak transient amplitudes (805.4 ± 150.6 pA, $n = 16$) and kinetic

properties (τ_{inact} = 587.7 ± 49.3 ms, τ_{deact} = 11.61 ± 2.8 ms) not unlike those reported for Kv1.3 alone (Fadool et al., 1997; Fadool and Levitan, 1998). Co-expression with any of the three sgRNAs, however, caused a significant reduction in voltage-activated Kv1.3 current amplitude (Fig. 2*D*, one-way ANOVA, $F_{(3,29)} = 6.679$, $^{**}p = 0.0014$). Because all three sgRNA constructs were equally effective in reducing Kv1.3 current amplitude, sgRNA1 was selected for *in vivo* use because of its proximity to the start codon.

We next performed an AAV serotyping assay in Tbx21-Cre mice to determine the vector with the highest transduction efficiency to deliver sgRNA to M/TCs *in vivo*. AAV2/xhSynEGFP (x = 2,5,6,8,9) was intracranially delivered to the MCL and allowed to express for six weeks before histologic analyses across the OB neurolaminae (Fig. 3*A*). At least two mice were examined for each serotype. AAV2 expression predominantly clustered around the injection site, and sparsely distributed expression across the bulb. AAV5 and AAV8 demonstrated the most localized expression to the granule cell layer (GCL). AAV5 labeled regularly along the MCL, while AAV8 labeled cells within the external plexiform layer (EPL) and glomerular layer (GLM). AAV6 labeling was restricted to the GLM. AAV9 labeled the MCL similarly to AAV5, but more robustly. To address the limitation of conically delivering an injectate to the center of a sphere, we investigated a retrograde variant of AAV2 (AAV2/retro). We injected this serotyping virus into the piriform cortex, hoping to effectively label M/TCs through retrograde transport. Although this approach effectively labeled cell bodies in the GLM, the density of labeling and reliability of transduction were lesser compared with direct injection of AAV9. We therefore selected AAV9 as the best vector to deliver our sgRNA1 for *in vivo* editing of *Kv1.3* in M/TCs.

The second goal was conditional expression of Cas9 in M/TCs. Tbx21-Cre mice are a useful tool to restrict expression of Cre recombinase to M/TCs (Haddad et al., 2013; Short and Wachowiak, 2019). Mating Tbx21-Cre mice to floxed Cas9/GFP mice generated progeny with Cas9/GFP expression limited to the M/TCs (Fig. 3*B*, left schematic). Using exposure-matched control images, we verified that there was no Cas9/GFP expression outside the OB in other regions of the brain, including that of the suprachiasmatic nucleus (SCN) of the hypothalamus (Fig. 4). To achieve maximal transduction of M/TCs across the OB, we further optimized AAV9 delivery by using a RO intravenous injection (Foust et al., 2009; Yardeni et al., 2011) to deliver our packaged sgRNA1 as AAV9-hSyn-mCherry-U6-sgRNA1 (Fig. 3*B*, right photomicrographs). The top photomicrograph is representative of the Cas9 expression in the Tbx21-Cre x Cas9/GFP mice, revealing restricted expression to the M/TCs layers (green channel, 488-nm excitation). The bottom photomicrograph shows the broad expression of the RO-delivered sgRNA1 (red channel, 594-nm excitation, magenta pseudo-colored, plus green channel merge; yellow co-labeled). The mCherry sgRNA reporter is prone to express in dispersed puncta, and typically does not neatly fill cell bodies (Costantini et al., 2015). Seventy-

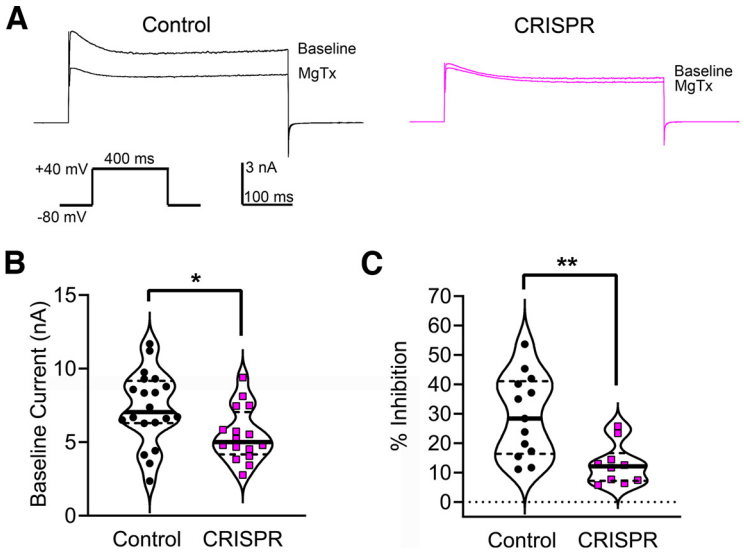

Figure 8. Inhibition of MC outward currents in Control versus CRISPR mice by a selective blocker of Kv1.3. ***A***, Representative records acquired from mitral cells that were voltage-clamped in the whole-cell configuration before (Baseline) and after the bath addition of 1 nM MgTx. Left, Control (Cas9(–) with sgRNA) mitral cell (MC). Right, CRISPR (Cas9(+) with sgRNA) MC. $V_h = -80$ mV, cells stepped to $V_c = +40$ mV with $P_d = 1000$ ms and IPI of 45 s. ***B***, Violin plot of the baseline voltage-activated peak transient current in Control (●) versus CRISPR (■) MCs. Student's *t* test, $^{*}p = 0.0215$. ***C***, Same as in ***B*** but for percent inhibition of the peak transient current magnitude by 1 nM MgTx for Control versus CRISPR MCs. *t* test with Welch's correction, $^{**}p = 0.0015$.

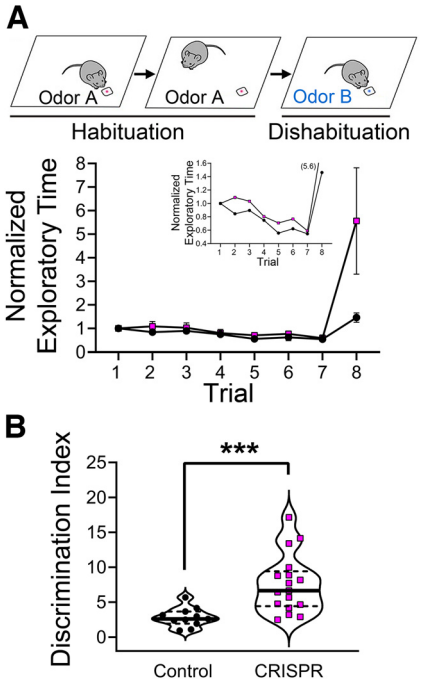

Figure 9. Odor habituation/dishabituation behavior in Control versus CRISPR mice. ***A***, Top, Cartoon demonstrating the habituation/dishabituation experimental paradigm whereby a mouse is repeatedly presented Odor A (left) until it loses exploration (center) and is habituated. At this point, it is presented with a novel Odor B (right) to assess whether it discriminates the cue from Odor A. Bottom, Line graph of the mean (±SEM) exploratory time per trial for Control (●) versus CRISPR (■) mice. Inset, Refined scale to visual habituation phase. ***B***, Violin plot of the DI for a population of Control versus CRISPR mice tested as in ***A***. DI is calculated as the normalized exploratory time from trial 8 divided by the normalized time from trial 7. Mann–Whitney *U*, $^{***}p = 0.0001$. Further behavioral phenotyping of the Control versus CRISPR mice with regards to foraging behavior and anxiety related to odor behavior can be found in Figure 10.

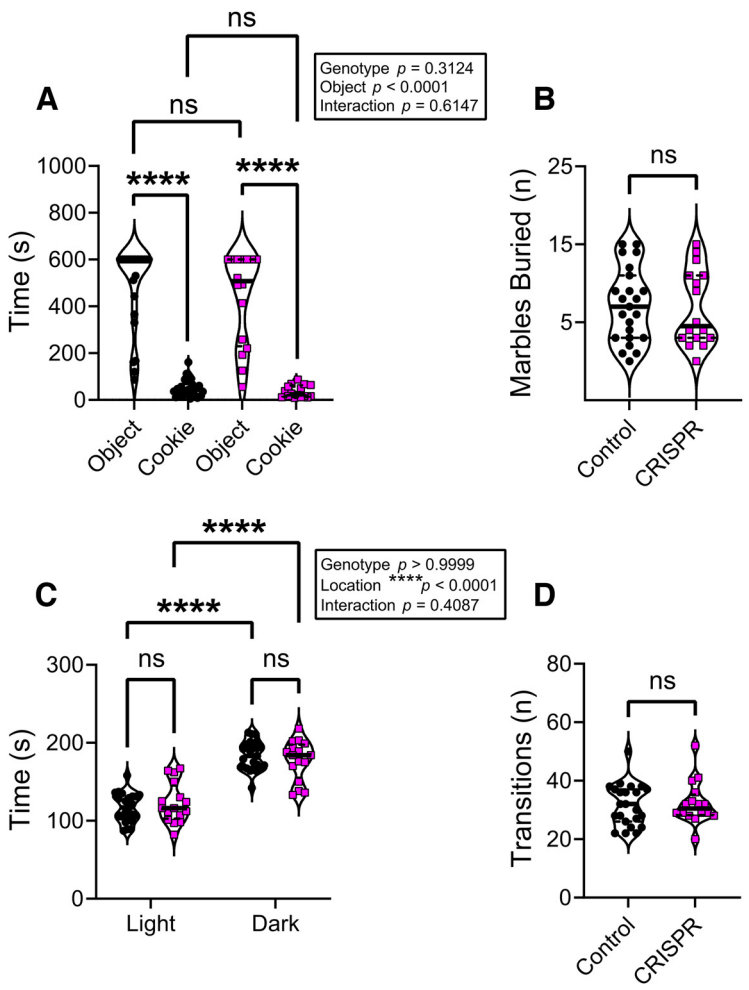

Figure 10. Buried cookie, marble burying, and LDB behaviors in Control versus CRISPR mice. ***A***, Violin plot of time spent to retrieve an unscented object (Object) or a peanut butter cookie (Cookie). comparing two-way mixed RM ANOVA with genotype and object as factors. ***B***, Violin plot of number of buried marbles as an indication of obsessive compulsive-like anxiety behavior. Student's *t* test. ***C***, Violin plot of time spent in light versus dark compartment of a LDB as an indication of anxiety-like behavior. Two-way mixed RM ANOVA with genotype and location as factors. ***D***, Violin plot of the number of transitions between light and dark compartments of the LDB as an indication of mobility. Student's *t* test. ***A–D***, Sample sizes are number of mice: Control (●) (23) CRISPR (■; 16). ns = not significantly different means, $^{****}p \leq 0.0001$.

seven fields of view across three Tbx21-Cre x Cas9/GFP mice that were RO-injected with sgRNA1 were examined at 63× magnification by laser confocal scanning microscopy (Fig. 3*C*). To determine the scale of CRISPR gene editing, we quantified the degree of Cas9/sgRNA1 co-labeling in MCs and TCs, respectively. We observed nearly 67% of MCs were co-labeled (67.4 ± 1.7%), whereas a lesser number of TCs (23.7 ± 4.6%) were co-labeled (Fig. 3*D*). Tbx21-Cre x Cas9/GFP progeny mice that are Cas9(+) and RO-injected with sgRNA virus will be referred to as "CRISPR mice" for the sake of brevity. Similarly, progeny that are Cas9(-) and RO-injected with sgRNA virus will be referred to as "Control mice."

After RO-injection of Tbx21-Cre x Cas9/GFP mice at age P5, at least 14 d were allowed to pass before performing *ex vivo* slice electrophysiology. This latency period was designed to allow for complete protein turnover of Kv1.3 after successful CRISPR editing within M/TCs. The effect of Kv1.3 germline deletion on the excitability of MCs has been well characterized (Fadool et al., 2004, 2011; Tucker et al., 2010; Mast and Fadool, 2012). We therefore compared RMP, evoked AP frequency, perithreshold current to induce firing (rheobase), and AP shape between CRISPR versus Control mice. As shown in Figure 5*A*, MCs of CRISPR mice had a less negative RMP [Control = −49.6 ± 4.5 mV (26) vs CRISPR = −46.5 ± 3.9 mV (35), Student's *t* test, $^{**}p = 0.0027$]. The number in parenthesis in this, and subsequent electrophysiological results, represents number of cells recorded. Following sampling of RMP, MCs were current-clamped using a holding potential (V_h) of −60 mV to allow comparison of threshold current required to evoke an AP. Using step-wise current injections of 25 pA (−50 to 200 pA, the determination of first evoked AP was made (Fig. 5*B*). The current needed to observe the first evoked APs was lower in CRISPR mice [Control = 96.9 ± 42.7 mV (16) vs CRISPR = 62.5 ± 42.0 mV (26), Mann–Whitney *U*, $^{*}p = 0.0195$]. The mean firing frequency in response to graded step depolarizations of short duration ranging from 0 to 225 pA showed a main effect of current on spikes/s (Fig. 5*C*, two-way mixed RM ANOVA using current and genotype as factors, $F_{(1.3,52.02)} = 118.6$, current $^{****}p < 0.0001$). In response to current injection, CRISPR MCs mice exhibited a higher spike firing frequency versus Control MCs, demonstrating a main effect of genotype (two-way mixed RM ANOVA, genotype $F_{(1,40)} = 5.176$, $^{*}p = 0.0283$, with a Sidak's *post hoc* test, $\#p = 0.0497$ at 150 pA). There was also a current × genotype interaction (two-way mixed RM ANOVA, $F_{(9,360)} = 3.440$, $^{***}p = 0.0004$, with a Sidak's *post hoc* test comparing to 25 pA, $\$\$p = 0.0033$, $\$\$\$p = 0.0003$, $\$\$\$\$p < 0.0001$). A violin plot of the increased spike firing frequency for CRISPR MCs at the 150-pA current step is shown in Figure 5*C* [right, Control = 12.8 ± 12.3 Hz (15) vs CRISPR = 28.5 ± 18.9 Hz (22), Mann–Whitney *U*, $^{**}p = 0.0090$]. Representative AP trains evoked by various current steps from a Control versus CRISPR mouse are shown in Figure 5*D*. The ISI and the peak instantaneous rate (PIR) showed a main effect of current (two-way mixed RM ANOVA, ISI = current $F_{(2.165,33.55)} = 15.77$, $^{****}p < 0.0001$; PIR = current $F_{(0.3402,5.273)} = 141.2$, $^{****}p = 0.0002$). Neither of these properties had a main effect of genotype, and therefore, no significant differences between MCs from CRISPR versus Control mice (Fig. 5*E*,*F*, two-way mixed RM ANOVA, ISI = genotype, $p = 0.3568$; PIR = genotype, $p = 0.8223$).

We next examined the AP shape of Control versus CRISPR MCs in response to a step depolarization evoked with 150-pA current from a V_h = −60 mV. APs acquired from CRISPR MCs exhibited a significantly faster time to rise to half amplitude [Fig. 6*A*, Control = 5.17 ± 0.05 ms (13) vs CRISPR = 5.05 ± 0.13 ms (12), Student's *t* test with Welch's correction, $^{**}p = 0.0093$]. Additionally, both the 10–90% rise time and the maximum rise slope were shorter and shallower, respectively, in recordings from CRISPR MCs [Fig. 6*B*,*C*, 10–90%, Control = 104.4 ± 37.1 ms (13) vs CRISPR = 70.1 ± 38.1 ms (12), Mann–Whitney *U*, $^{*}p = 0.0457$; rise slope, Control = 138.0 ± 40.5 mV/ms (15) vs CRISPR = 110.3 ± 40.9 mV/ms (19), Mann–Whitney *U*, $^{*}p = 0.0396$].

Most notably, the repolarization kinetics were affected in a manner consistent with a loss of potassium channel conductances. The time to achieve maximum decay slope was lengthened in the APs of CRISPR MCs [Fig. 6*D*, Control = 0.62 ± 0.15 ms (15), CRISPR = 0.81 ± 0.24 ms (19), Student's *t* test, $^{*}p = 0.0125$].

We previously reported compensatory upregulation in the expression of other ion channels in whole-animal Kv1.3−/− mice. Because we now used CRISPR to postnatally edit *Kv1.3*, we anticipated that the CRISPR mice should not have any of the same compensation (Fadool et al., 2004; Lu et al., 2010). To confirm this, we compared Kv channel expression in isolated OB membranes or immunoprecipitates between Control and CRISPR mice using SDS-PAGE and Western blot analysis. Quantitative densitometry was performed in triplicate for each channel of interest, where pixel density was computed as a Cas9(+)/Cas9(−) ratio normalized to $\alpha\beta$ Tubulin III (BTub) loading control (Fig. 7). Pixel immunodensity of immunoprecipitated Kv1.3 channel protein (58 kDa) in CRISPR mice was significantly reduced compared with that of Control mice (Student's *t* test with arcsine transformation, $^{**}p = 0.0022$), which was consistent with selective genome editing of the *Kv1.3* from M/TCs in the OB (Fig. 7*A*). Conversely, immunodensity values comparing other *Shaker* family members (Kv1.4, Kv1.5), a sodium-activated K channel (Slack B), or the β subunit of the sodium channel (Nab) were not significantly different in membrane preparations between Control and CRISPR mice (Fig. 7*B*, Kv1.4 $p = 0.5483$, Kv1.5 $p = 0.6453$, Slack B $p = 0.6773$, Nab $p = 0.9147$). CRISPR mice therefore did not show any compensatory upregulation in the examined voltage-gated ion channels (Fig. 7*C*) that could have modified excitability.

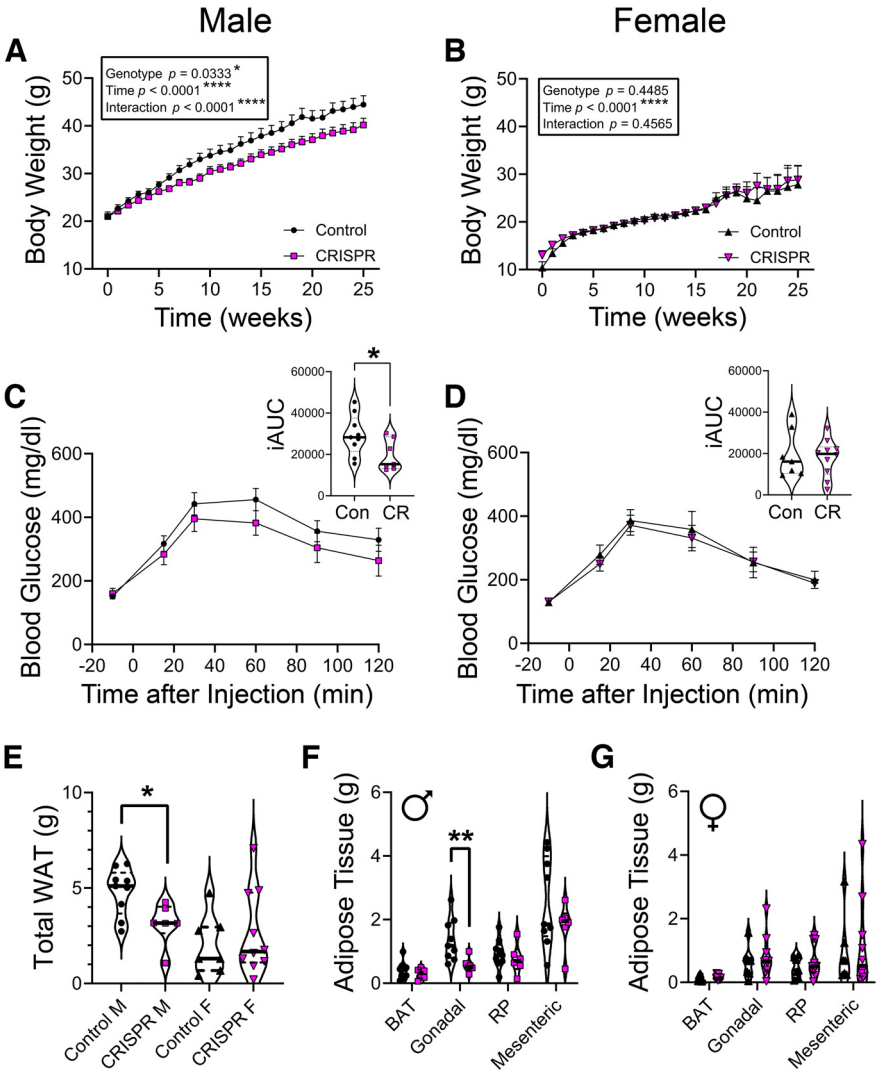

Figure 11. Obesity response of CRISPR mice to a 25-week MHF challenge. Line graph of the mean (±SEM) body weight gain over time for (***A***) male and (***B***) female mice comparing Control (●) versus CRISPR (■). Two-way mixed RM ANOVA with genotype and time as factors. Sample sizes are number of mice: Control male (12), CRISPR male (13), Control female (7), and CRISPR female (10). Line graph of the mean (±SEM) blood glucose over time for (***C***) male and (***D***) female mice comparing Control versus CRISPR. Inset, iAUC for Control (Con) males versus CRISPR (CR) males. Student's *t* test, $^{*}p = 0.0479$. ***E***, Violin plots comparing total white adipose tissue (WAT) deposition for Control versus CRISPR males (M) and females (***F***), respectively. Student's *t* test, $^{*}p = 0.0178$. Violin plots showing the deposition of adipose tissue in (***F***) male and (***G***) female Control versus CRISPR mice. *t* test with Welch's correction, $^{**}p = 0.0079$. BAT = brown adipose tissue, RP = retroperitoneal. Body weight and blood glucose measurements of nonobese CRISPR mice maintained on CF diet can be found alternatively in Figure 12.

To support our biochemical findings, we predicted that loss of Kv1.3 should reduce the amplitude of isolated voltage-activated outward currents. Moreover, if genome editing was selective to *Kv1.3*, then a selective vestibule blocker of Kv1.3 could be used to demonstrate differential inhibition between Control and CRISPR recordings. MgTx binds the open vestibule of Kv1.3, and at 1 nM, MgTx is a selective inhibitor of Kv1.2 and Kv1.3 (Bartok et al., 2014; Schwartz et al., 2017). We therefore measured voltage-activated outward currents in Control and CRISPR MCs in response to a single step depolarization from $V_m = -80$ mV to $V_c = +40$ mV (Fig. 8*A*). Upon achieving the whole-cell configuration, TTX was bath-applied to eliminate unwanted inward sodium currents, and then a baseline recording was performed for 5 min. Peak transient currents were compared at the $V_c = +40$-mV step, and it was found that CRISPR mice had significantly less outward current [Fig. 8*B*, Control = 7.3 ± 2.5 nA (20) vs CRISPR = 5.5 ± 1.8 nA (16), Student's *t* test, $^{*}p = 0.0215$]. At the 15-min recording time, MgTx was introduced to the bath and was allowed to wash over the slice for 15 min as necessary for the slow K_{on} of the peptide blocker (Fadool and Levitan, 1998; Schwartz et al., 2017, 2021). The voltage-activated outward currents of CRISPR MCs were resistant to MgTx inhibition versus that observed for Control MCs [Fig. 8*A*,*C*, Control = 29.3 ± 13.9% (13) vs CRISPR = 12.8 ± 6.9% (10), *t* test with Welch's correction, $^{**}p = 0.0015$]. The observed lack of MgTx sensitivity is consistent with selective Kv1.3 editing.

CRISPR mice have improved odor discrimination in a habituation/dishabituation assay

We next performed olfactory assessment on CRISPR mice using an odor habituation-dishabituation paradigm to determine changes in olfactory discrimination. Whole-animal Kv1.3−/− mice show a 4- to 30-fold increase in olfactory discrimination, depending on the odorant pair used for testing (Fadool et al.,

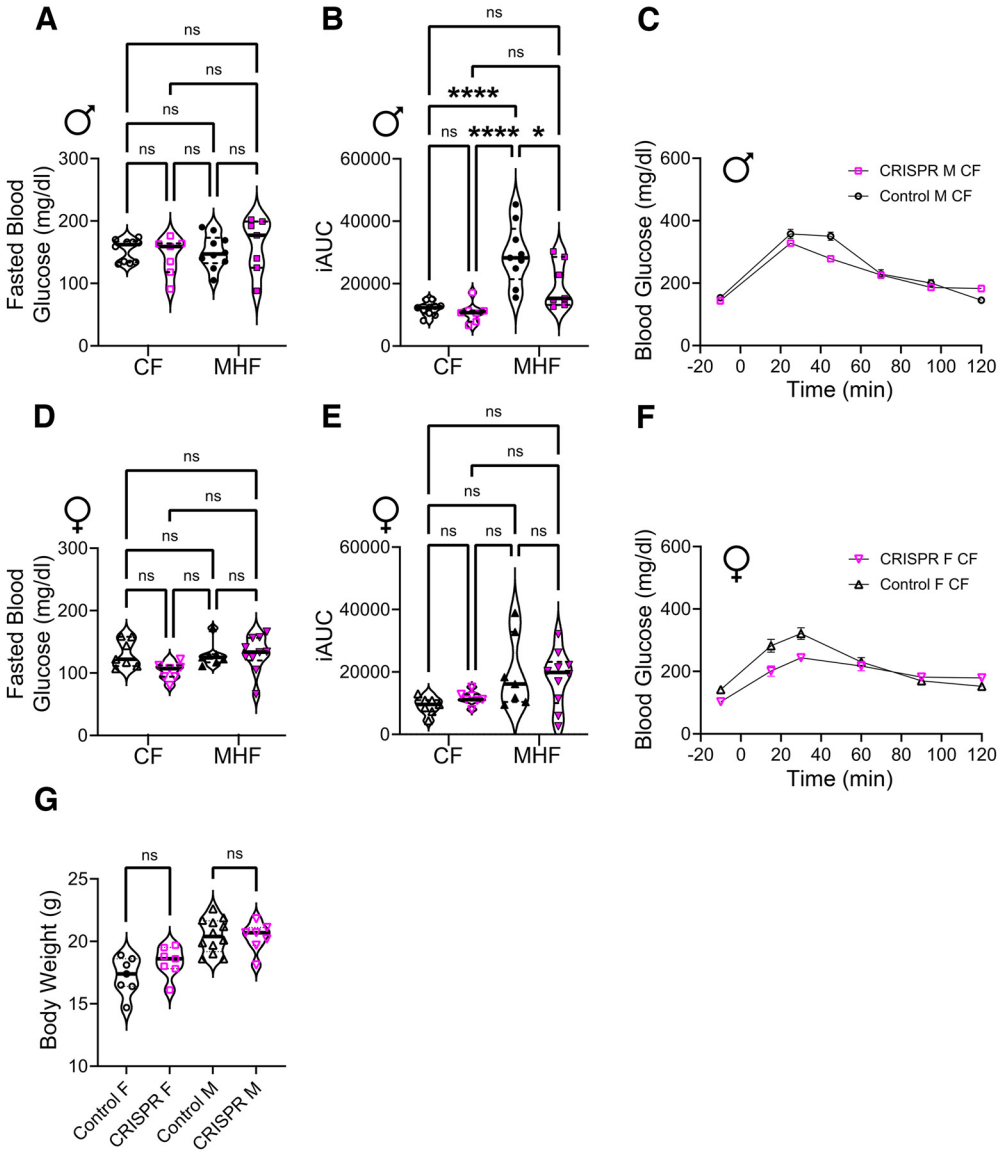

Figure 12. Blood glucose and body weight measurements in CRISPR mice maintained on CF diet in comparison to a 25-week MHF challenge. ***A***, Violin plot of fasted blood glucose comparing Control (●) versus CRISPR (■) male mice in response to a CF or a MHF challenge (MHF) as in Figure 11. Two-way ANOVA with genotype and diet as factors. Sample sizes are number of mice: Control CF (10), CRISPR CF (7), Control MHF (10), and CRISPR MHF (7). ***B***, Violin plot of iAUC for blood glucose clearance over time as in Figure 11 and ***C***. Two-way ANOVA with genotype and diet as factors. Sidak's *post hoc* test, $^{*}p = 0.0345$, $^{****}p < 0.0001$. ***C***, Line graph of the mean (±SEM) blood glucose over time for male mice comparing Control versus CRISPR on CF diet. ***D–F***, Same as ***A–C*** but for females. Sample sizes are number of mice: Control CF (7), CRISPR CF (7), Control MHF (7), and CRISPR MHF (10). ***G***, Violin plot of body weight of Control versus CRISPR mice maintained on CF diet. Student's *t* test within sex, $p > 0.05$, ns = not significantly different. F = female, M = male. Sample sizes are number of mice: Control F (7), CRISPR F (7), Control M (12), and CRISPR M (7).

2004). In this paradigm, the time that a mouse spends exploring an odor is used to infer whether a mouse can recognize that odor as novel. Mice were presented an odor stimulus at regular intervals, and their exploratory time was recorded (habituation). After seven trials with Odor A, a contrasting Odor B was presented (dishabituation). The experimental paradigm and normalized exploratory values are shown in Figure 9*A*. The mean exploratory time for the first odor exploration was not significantly different between the Control and CRISPR animals [3.2 ± 1.4 s. Control (11) vs CRISPR 4.1 ± 1.3 s (17), Student's *t* test, $p = 0.1815$]. For graphing purposes, all recorded times were normalized to the animal's original exploration time before habituation (trial 1) to minimize between-animal variance as in Tucker et al., (2012b). The exploratory time of Odor B was then divided by the habituated exploratory time of Odor A (trial 7) to determine the discrimination index (DI). CRISPR mice showed a significantly greater DI, and therefore had greater olfactory discrimination versus Control littermates [Fig. 9*B*, Control DI = 2.8 ± 1.4 (11) vs CRISPR DI = 7.6 ± 4.2 (17), Mann–Whitney *U*, $^{***}p = 0.0001$].

Although gross anosmia testing may not be able to detect fine changes in discrimination, it does allow detection of foraging activity. We therefore also examined the ability of CRISPR versus Control littermates to discover a buried peanut butter cookie over that of an unscented object (Tucker et al., 2012b). CRISPR and control littermates were able to retrieve buried food under a similar time course and did not uncover unscented objects differently [time to retrieve unscented object Control = 483 ± 37 s (23) vs CRISPR = 436 ± 48 s (16); time to retrieve cookie Control = 51 ± 8 s (23) vs CRISPR = 36 ± 6 s (16)]. A two-way mixed RM ANOVA

showed a main effect of object where both mice retrieved the cookie significantly faster than the unscented object without a genotypic difference (object $F_{(1,37)} = 177.2$, $^{****}p < 0.0001$; genotype $F_{(1,37)} = 1.049$, $p = 0.3124$; object × genotype interaction $F_{(1,37)} = 0.2577$, $p = 0.6147$). These data suggest that the increased odor discrimination of CRISPR mice is not mediated by a difference in foraging behavior (Fig. 10*A*).

Previously in using whole-animal Kv1.3 knock-out mice, we observed increased anxiety-like behavior consecutive to an enhanced olfactory, "super-smeller" phenotype (Fadool et al., 2004; Huang et al., 2018). We therefore tested anxiety-like behavior using two paradigms – marble burying test and the LDB. CRISPR mice did not bury more marbles than that of Control littermates [Control = 7.2 ± 4.7 (23) marbles vs CRISPR = 6.8 ± 4.9 (16) marbles, Student's *t* test, $p = 0.8264$; Fig. 10*B*]. Both mice preferred the dark side over that of the light in the LDB and there was no main effect of genotype [Control Dark Time = 183 ± 19 s (23) vs CRISPR Dark Time = 177 ± 26 s (16); 2w RM mixed ANOVA; compartment location $F_{(1,37)} = 73.14$, $^{****}p < 0.0001$; genotype $F_{(1,37)} = 0.000$, $p > 0.9999$; location × genotype interaction $F_{(1,37)} = 0.6983$, $p = 0.4087$; Fig. 10*C*]. Moreover, CRISPR mice did not have significantly different number of transitions between compartments compared with that of Control mice, signifying similar locomotor activity during the task [Control = 32 ± 7 (23) transitions vs CRISPR = 32 ± 7 (16) transitions, Student's *t* test, $p = 0.8080$; Fig. 10*D*]. These results suggest that targeted loss of Kv1.3 in mitral cells alone does not result in increased anxiolytic tendencies.

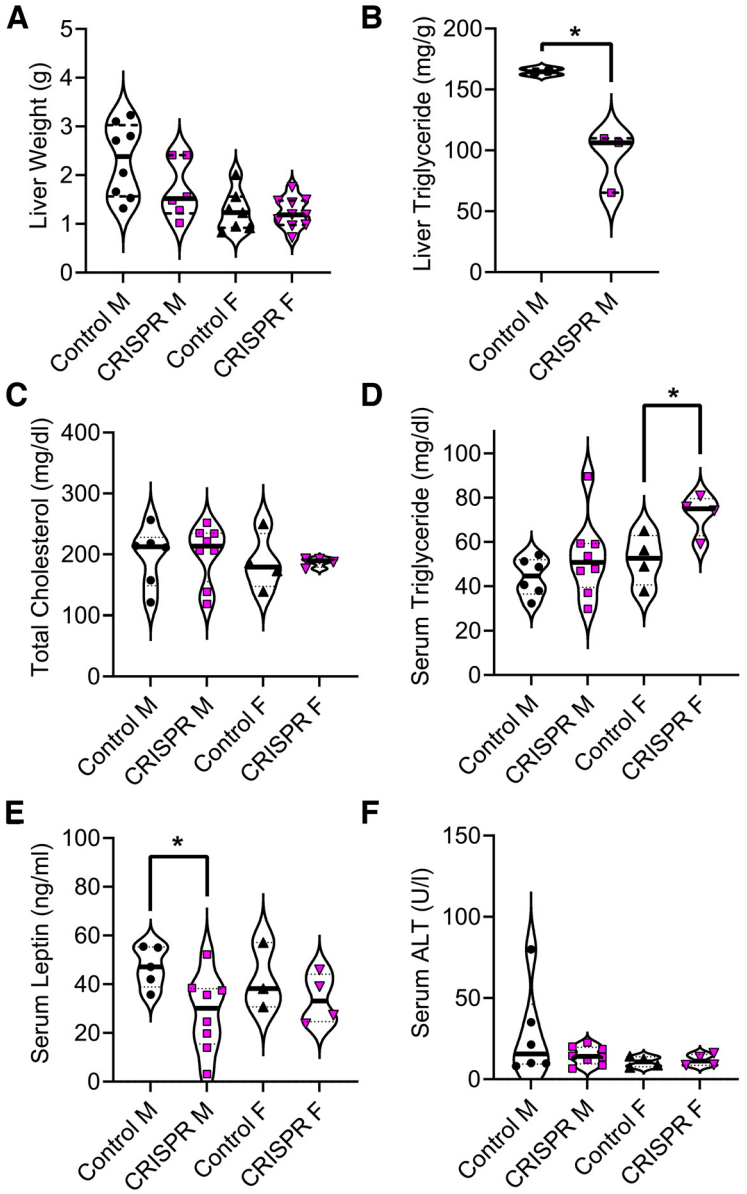

Figure 13. Analysis of obesity markers from liver tissue and blood serum taken from Control versus CRISPR mice following a 25-week MHF challenge. ***A***, Violin plots comparing total liver weights for Control (●) versus CRISPR (■) males (M) and females (F), respectively. ***B***, Violin plot comparing triglyceride content per gram of liver tissue, Control versus CRISPR males. *t* test with Welch's correction, $^{*}p = 0.0353$. Violin plots comparing (***C***) serum cholesterol content, (***D***) serum triglyceride content (Student's *t* test, $^{*}p = 0.0334$), (***E***) serum leptin concentration (Student's *t* test, $^{*}p = 0.0334$), and (***F***) serum alanine aminotransferase (ALT) for Control versus CRISPR mice.

CRISPR mice have improved metabolic health

Whole-animal knock-out of *Kv1.3* confers a resistance to DIO (Xu et al., 2003, 2004; Tucker et al., 2008, 2012a; Thiebaud et al., 2014). We therefore tested whether conditional gene inactivation of *Kv1.3* in M/TCs could replicate the same resistance to DIO. Moreover, previous work exploring DIO resistance in Kv1.3−/− models, or using mice treated with Kv1.3 inhibitors, had been restricted to just male mice (Xu et al., 2003; Tucker et al., 2008, 2012a; Upadhyay et al., 2013; Thiebaud et al., 2014; Schwartz et al., 2021). We included female mice to determine whether any sex-specific effects could be noted. We performed a 25-week dietary challenge (as in Schwartz et al., 2021) wherein male and female CRISPR and Control mice were provided with a MHF diet of 32% fat on weaning. Male Control mice gained significantly more body weight than male CRISPR mice, which were more resistant to the DIO challenge (Fig. 11*A*, two-way mixed RM ANOVA, genotype $F_{(1,23)} = 5.128$, $^{*}p = 0.0333$; time × genotype interaction $F_{(25,575)} = 2.603$, $^{****}p < 0.0001$). Sidak's *post hoc* pair-wise comparisons did not indicate a significant effect of genotype at any individual time point (all $p > 0.05$). In contrast with the male mice, female Control mice did not show an increase in body weight in response to the MHF diet. As such, any resistance to obesity in female CRISPR mice could not be determined (Fig. 11*B*, two-way mixed RM ANOVA, genotype $F_{(1,15)} = 0.1733$, $p = 0.6831$). The lack of DIO in female mice has also been observed in C57BL6/J strains, so this was not unexpected (Chelette et al., 2022). Because increases in body weight can cause changes in glucose homeostasis and adipose deposition, we next examined these metrics that could indicate a prediabetic state. Consistent with the sexual dimorphism observed in body weight gain, Control male mice, but not female mice, had slower glucose clearance after a glucose challenge. Accordingly, the iAUC for CRISPR mice was significantly less than that of Control mice (Fig. 11*C*,*D*, males, Student's *t* test, $^{*}p = 0.0479$, $n = 17$; females,

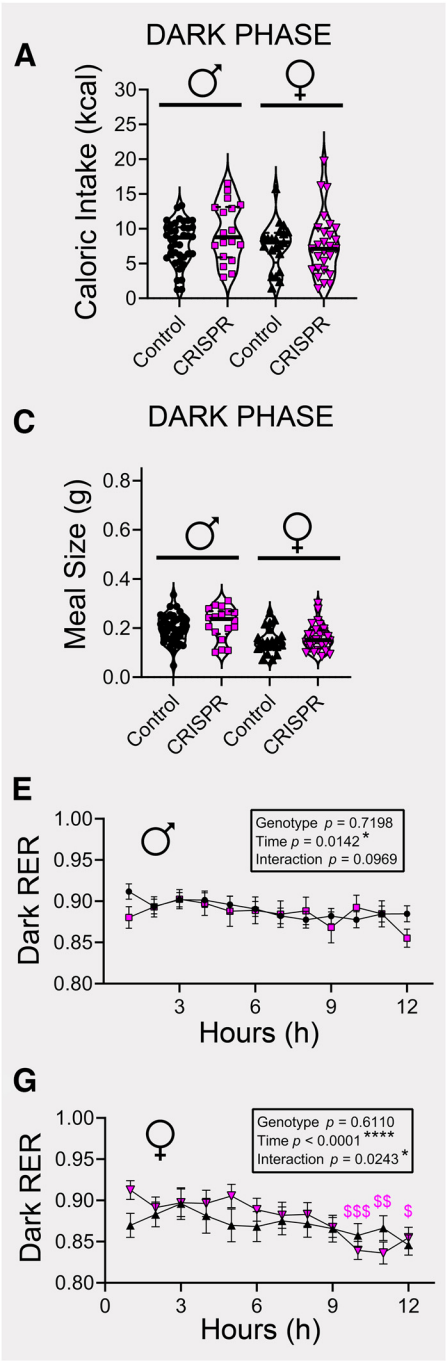

Figure 14. Metabolic assessment of CRISPR mice following a 25-week MHF challenge. Data were acquired in a CLAMS and are separated by dark phase (12-h "lights off" period, left column, gray background) and light phase (12-h "lights on" period, right column, white background). ***A***, ***B***, Violin plot of the total caloric intake over each 12/12 h light/dark phase for Control (●) versus CRISPR (■) mice, males and females. The same data reported in ***A***, ***B***, but normalized to the animal's body weight, can be found in Figure 15. ***C***, ***D***, Same as in ***A***, ***B***, but for average meal size. Light phase, males: Student's *t* test, $*p = 0.0436$; females: Student's *t* test, $p = 0.0227$. Line graph of the mean (±SEM) RER in Control versus CRISPR (***E***, ***F***) male and (***G***, ***H***) female mice. Two-way mixed RM ANOVA with genotype and time as factors. Sidak's *post hoc* test, $\$p < 0.05$, $\$\$p < 0.01$, $\$\$\$p < 0.001$, time × genotype interaction compared with 1-h time point. ***E–H***, Sample sizes are number of metabolic measurements: Control male (39), CRISPR male (18), Control female (21), and CRISPR female (27). Additional metabolic parameters compared between Control versus CRISPR mice can be found in tabled form in Extended Data Figure 14-1. A refined analysis of caloric intake/hour or normalized comparison of caloric intake and RER can be found in Figure 16.

Student's *t* test, $p = 0.7155$, $n = 17$). While the ability to clear a glucose challenge was improved for CRISPR mice, the fasting glucose levels between Control versus CRISPR mice in either sex were unchanged [males, Control = 150.6 ± 26.7 mg/dl (10) vs CRISPR = 160.4 ± 43.6 mg/dl (7), Student's *t* test, $p = 0.5716$; females, Control = 129.3 ± 19.9 mg/dl (7) vs CRISPR = 130.9 ± 29.1 mg/dl (10), $p = 0.7396$].

We next examined fat and lean tissue weight *in vivo* by eMRI, and analyzed within sex and across genotype. The lean tissue weight was approximately the same in both males and females, and there was no effect of genotype [males, Control = 25.47 ± 1.65 g (10) vs CRISPR = 24.95 ± 1.38 g (13), Student's *t* test, $p = 0.2847$; females, Control = 19.32 ± 1.22 g (10) vs CRISPR = 18.84 ± 1.64 g (13), Student's *t* test, $p = 0.5288$]. The fat tissue weight was greater in males as anticipated from the sexual dimorphism in BW, but there was not a significant effect of genotype in either sex [males, Control = 15.56 ± 3.03 g (10) vs CRISPR = 12.87 ± 4.68 g (13), Student's *t* test, $p = 0.2847$; females, Control = 3.96 ± 2.91 g (7) vs CRISPR = 6.07 ± 3.78 g (10), Student's *t* test, $p = 0.2338$]. The calculated percent body fat between Control versus CRISPR mice was also not significantly different [males, Control = 35.6 ± 4.6% (10) vs CRISPR = 33.2 ± 5.2% (13), Mann–Whitney *U*, $p = 0.2753$; females, Control = 14.9 ± 9.2% (7) vs CRISPR = 19.4 ± 9.8% (9), Mann–Whitney *U*, $p = 0.6065$].

We then examined adipose deposition postmortem to complement body composition data estimated from eMRI scanning. CRISPR males had less total WAT than that of Control mice [Control = 4.82 ± 1.24 g (9) vs CRISPR = 3.12 ± 1.11 g (6), Student's *t* test, $*p = 0.0178$], whereas females had no significant difference in WAT accumulation [Control = 2.02 ± 1.54 g (7) vs CRISPR = 2.62 ± 2.21 g (10), Student's *t* test $p = 0.5444$; Fig. 11*E*]. Further analysis of individual fat pads indicated that epididymal fat was significantly reduced in the CRISPR male mice (*t* test with Welch's correction, $**p = 0.0079$, $n = 15$), whereas brown fat, retroperitoneal, and mesenteric fat were not found to be significantly different (Fig. 11*F*). Female adipose storage was not significantly different between CRISPR and Control mice (Fig. 11*G*), regardless of deposition site.

The ability to clear a glucose challenge was improved for CRISPR mice over that of Control littermates while maintained on MHF chow. We therefore examined whether CRISPR editing could normalize glycemic curves to control values in mice maintained on a CF diet rather than when on an obesogenic diet. We performed IPGTT on a cohort of CRISPR versus Control littermates that were maintained on CF (mice were not obese), and compared glucose clearance

between both MHF-maintained and CF-maintained mice, within sex and across genotype. Interestingly, in male mice, CF-maintained CRISPR mice had an iAUC that was not significantly different from that of MHF-maintained CRISPR mice or CF-maintained Control mice (two-way ANOVA genotype $F_{(1,29)} = 5.761$, $^{*}p = 0.0230$; diet $F_{(1,29)} = 33.22$, $^{****}p < 0.0001$; Sidak's *post hoc* test for CRISPR CF vs MHF, $p = 0.0886$; Fig. 12*A–C*). In female mice, no differences were observed across diet or genotype for glucose clearance (Fig. 12*D–F*). These data suggest that our CRISPR genome editing may protect glucose clearance in obese, rather than normal weight, animals.

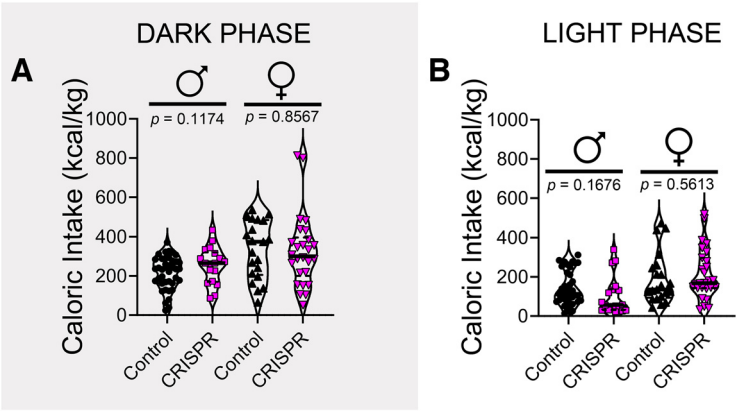

Figure 15. Metabolic assessment of CRISPR mice following a 25-week MHF challenge. Same as Figure 14*A,B* but reported normalized to the body weight of the animal in kilograms.

To further determine how the overall health of the CRISPR mice might be impacted, we performed gross tissue necropsy and examined blood markers. Total liver organ weight was not significantly different across CRISPR versus Control animals in either sex [Fig. 13*A*, males, Control = 2.3 ± 0.75 g (8) vs CRISPR = 1.7 ± 0.59 g (6), Student's *t* test, $p = 0.1279$; females, Control = 1.3 ± 0.42 g (7) vs CRISPR = 1.2 ± 0.31 g (10), Student's *t* test, $p = 0.8617$]. Liver triglycerides, however, were found to be significantly reduced in CRISPR males versus Control animals [Fig. 13*B*, Control = 164.7 ± 3.5 mg/g (2) vs CRISPR = 93.8 ± 24.8 mg/g (3), Student's *t* test with Welch's correction, $^{*}p = 0.0353$]. Females were not available for liver triglyceride analysis. We then collected blood from both sexes, and prepared serum using a standard centrifugation protocol (Chejfec, 2001). Serum total cholesterol was not significantly different between CRISPR and Control mice for either sex [Fig. 13*C*, males, Control = 196.4 ± 48.5 mg/dl (6) vs CRISPR = 201.4 ± 47.8 mg/dl (8), Student's *t* test, $p = 0.8515$; emales, Control = 187.0 ± 46.5 mg/dl (4) vs CRISPR = 187.0 ± 7.6 mg/dl (4), Student's *t* test with Welch's correction, $p > 0.9999$]. Unexpectedly, serum triglycerides did not differ in males but were significantly elevated in CRISPR females [Fig. 13*D*, males, Control = 44.1 ± 8.5 mg/dl (6) vs CRISPR = 52.9 ± 18.0 mg/dl (8), Student's *t* test with Welch's correction, $p = 0.2543$; females, Control = 52.0 ± 11.5 mg/dl (4) vs CRISPR = 72.4 ± 9.4 mg/dl (4), Student's *t* test, $^{*}p = 0.0334$]. Serum leptin levels were significantly lower in male CRISPR versus Control mice, but did not reach statistical significance in female mice [Fig. 13*E*, males, Control = 47.07 ± 8.50 ng/ml (5) vs CRISPR = 28.17 ± 15.75 ng/ml (8), Student's *t* test, $^{*}p = 0.0326$; females, Control = 42.00 ± 13.62 ng/ml (3) vs CRISPR = 33.96 ± 10.26 ng/ml (4), Student's *t* test, $p = 0.4101$]. Serum alanine aminotransferase (ALT) was not significantly different between CRISPR and Control mice for either sex [Fig. 13*F*, males, Control = 27.3 ± 27.7 U/L (6) vs CRISPR = 14.5 ± 5.6 U/L (8), *t* test with Welch's correction, $p = 0.3134$; females, Control = 10.7 ± 3.2 U/L (4) vs CRISPR = 11.7 ± 3.7 U/L (4), Student's *t* test, $p = 0.6959$].

We anticipated distinct metabolic function in CRISPR mice, given their observed changes in adipose deposition, total serum triglycerides, and in liver lipids. We used a CLAMS to physiologically profile metabolic gas consumption/production, movement activity, heat generation, and feeding and drinking behaviors in the mice. Total food intake and average meal size were assessed for each 12-h dark and 12-h light phase, respectively. Daily 12-h caloric intake did not significantly differ between CRISPR versus Control animals during the dark [Fig. 14*A*, males, Control = 8.0 ± 3.1 kcal (39) vs CRISPR = 9.5 ± 4.2 kcal (18), Student's *t* test, $p = 0.1207$; females, Control = 7.5 ± 3.3 kcal (21) vs CRISPR = 7.7 ± 4.5 kcal (27), Student's *t* test, $p = 0.8998$] or light phase [Fig. 14*B*, males, Control = 5.4 ± 3.5 kcal (39) vs CRISPR = 3.7 ± 3.4 kcal (18), Student's *t* test, $p = 0.0995$; females, Control = 4.2 ± 2.6 kcal (21) vs CRISPR = 4.5 ± 2.9 kcal (27), Student's *t* test, $p = 0.6750$]. This was the same whether or not the caloric intake was normalized to that of the weight of the animal (Fig. 15*A,B*). We also examined the average meal size of the mice to determine whether there was a change in eating behavior rather than total caloric consumption. This was not significantly different during the dark phase (Fig. 14*C,D*, Student's *t* test, $p > 0.05$). During the light phase, however, CRISPR males consumed smaller meals versus those of Controls, and CRISPR females consumed larger meals versus those of Controls [Fig. 14*D*, males, Control = 0.21 ± 0.10 g (39) vs CRISPR = 0.16 ± 0.05 g (18), Student's *t* test, $^{*}p = 0.0436$; females, Control = 0.13 ± 0.04 g (21) vs CRISPR = 0.19 ± 0.11 g (27), Student's *t* test, $^{*}p = 0.0227$].

Next, we calculated the RER during the dark and light phases and compared the computed value within sex and across genotype. RER is the ratio between the metabolic production of CO_2 and the consumption of O_2, and can be used to infer metabolic substrate utilization. For the male mice, there was a main effect of time across both the dark and light phases for RER (Fig. 14*E,F*, two-way RM ANOVA, dark, time $F_{(4.771,291.0)} = 2.838$, $^{****}p < 0.0001$; light, time $F_{(4.771,291.0)} = 2.838$, time $^{*}p < 0.0177$), which was likely circadian in nature. During the dark phase, there was no significant difference in RER between CRISPR and Control mice (Fig. 14*E*, two-way mixed RM ANOVA, $F_{(1,65)} = 0.1299$, genotype $p = 0.7198$). During the light phase, however, there was a significant reduction in RER in the CRISPR mice, and a time × genotype interaction (Fig. 14*F*, two-way mixed RM ANOVA, genotype $F_{(1,61)} = 4.450$, $^{*}p = 0.0390$; time × genotype interaction $F_{(11,715)} = 1.590$, $^{*}p = 0.0253$, Sidak's *post hoc* test, $\$p < 0.05$, $\$\$p < 0.01$, $\$\$\$p < 0.001$). Sidak's *post hoc* pair-wise comparisons did not indicate a significant effect of genotype at any individual time point (all $p > 0.05$). This downward shift in RER represents an increase in the metabolic use of fats, relative to total substrate use. In the female mice, we also observed an effect of time for RER across both the dark and light phases (Fig. 14*G,H*, two-way RM ANOVA, dark, time $F_{(6.033,301.7)} = 5.913$, time $^{****}p < 0.0001$; light, time $F_{(11,506)} = 2.188$, time $^{*}p = 0.0140$).

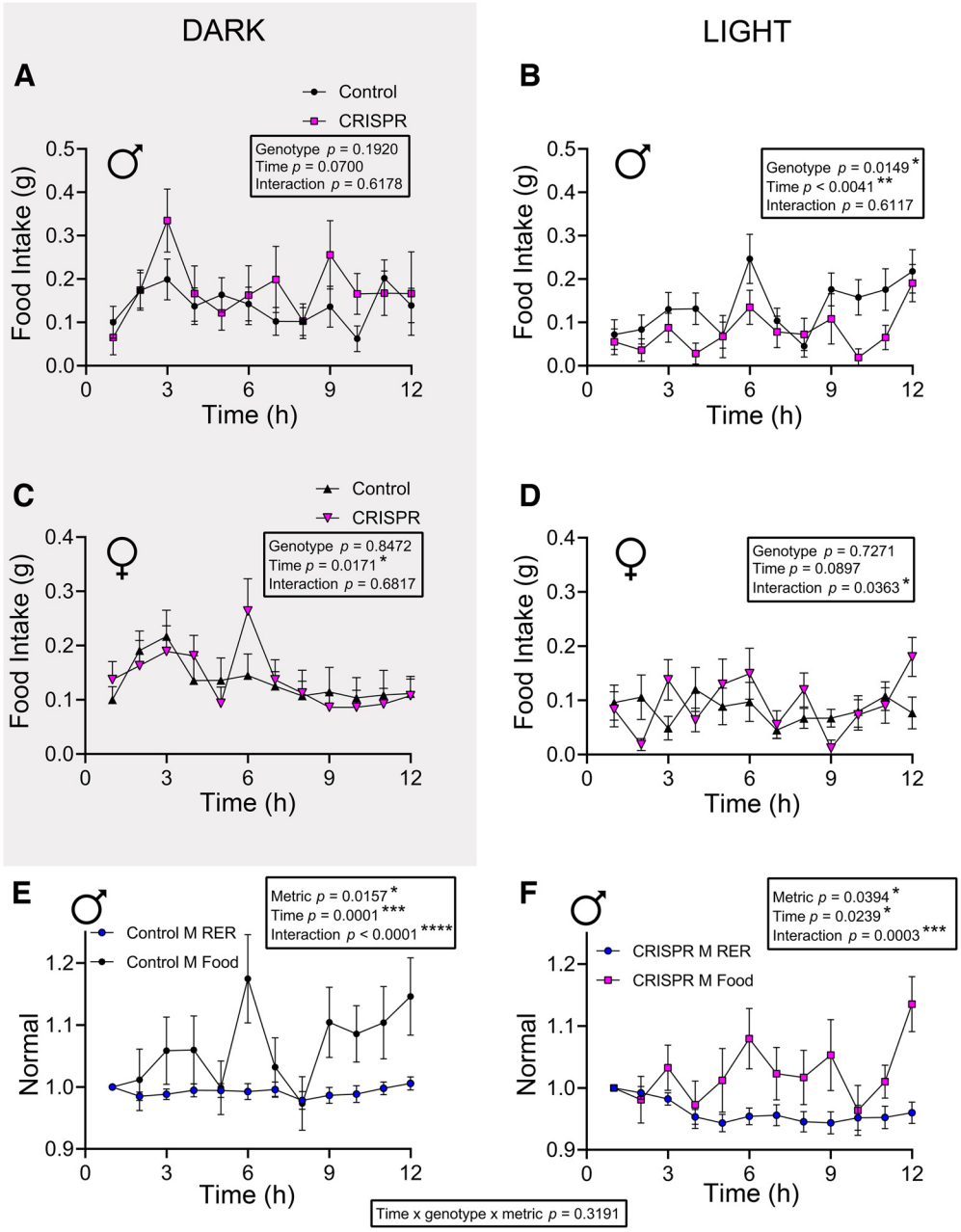

Figure 16. Food intake and RER in CRISPR mice assessed as in Figure 14, but reported over time or normalized to each other. Line graph of the mean (±SEM) food intake for Control (●) versus CRISPR (■) male (***A***, ***B***) and female (***C***, ***D***) mice. Two-way mixed RM ANOVA with genotype and time as factors. Results of ANOVA reported on the figure. Sidak's *post hoc* test *ns*, $p \geq 0.05$. Note shading representing light/dark phase. ***E***, ***F***, Line graph of RER and food intake for male mice in the light phase normalized to the 1-h time point. Two-way mixed RM ANOVA with physiologic metric and time as factors. Results of ANOVA reported on the figure. Sidak's *post hoc* test \$$p < 0.05$, \$\$$p < 0.01$, \$\$\$\$$p < 0.0001$. Data were plotted within genotype for clarity, reporting Control (***E***) and CRISPR (***F***) independently, and then were analyzed by three-way mixed RM ANOVA to detect any metric × time × genotype interaction, which was not found to be significant (see box between ***E*** and ***F***; $p = 0.3191$).

In the dark phase, a time × genotype interaction was observed wherein RER was elevated early evening in CRISPR females, and then dropped below that of the Control mice toward the onset of the light phase (Fig. 14*G*, two-way mixed RM ANOVA, time × genotype interaction $F_{(11,550)} = 2.025$, $^*p = 0.0243$ with a Sidak's *post hoc* test, \$$p < 0.05$, \$\$$p < 0.01$, \$\$\$$p < 0.001$). In the light phase, there was no effect of genotype nor a time × genotype interaction in the female mice (Fig. 14*H*, two-way mixed RM ANOVA, $p > 0.05$). None of the other metabolic metrics that we examined (daily water consumption, locomotor activity, heat expenditure, or gas exchange) were significantly different between CRISPR versus Control animals analyzed within sex and within light/dark phase (see Extended Data Fig. 14-1, Student's *t* test, $p > 0.05$).

Despite a lack of change in 12-h total caloric intake across genotypes, we examined whether there was a difference in the hourly time course of food intake (Fig. 16*A*) such as was observed in the whole-body Kv1.3-null mice (Fadool et al., 2004). When examined over the course of the day, male CRISPR animals ate less during the light cycle than Control animals, and this behavior was restricted to the light, and not the dark cycle (Fig. 16*A*,*B*; two-way mixed RM ANOVA, main effect of time and genotype as factors; genotype $F_{(1,37)} = 6.517$, $p = 0.0149$; time $F_{(6.593,244)} = 3.148$,

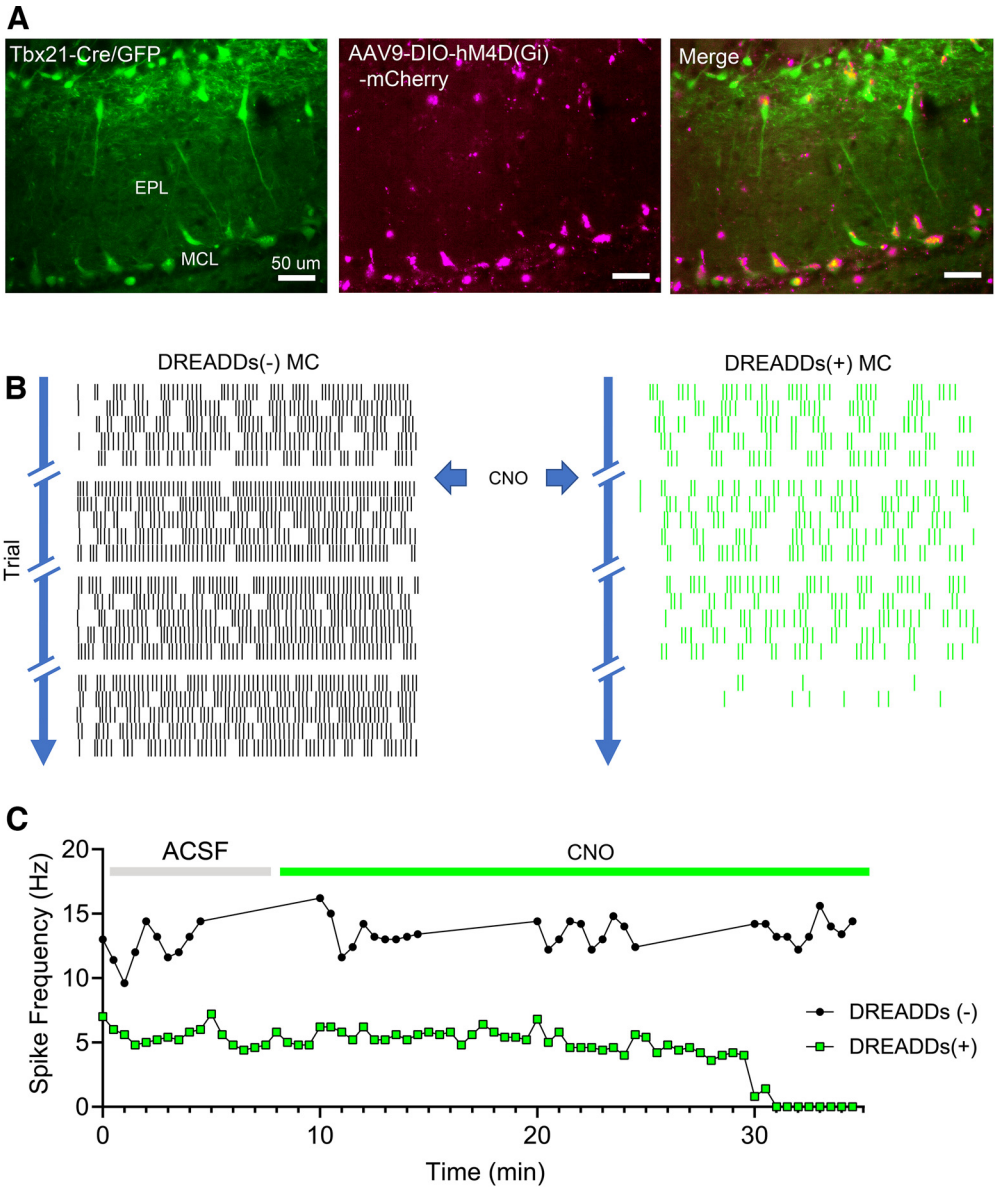

Figure 17. Development and *ex vivo* verification of inhibitory DREADDs mice. ***A***, Left, Photomicrograph of a representative OB coronal section from a Tbx21-Cre x Cas9/GFP progeny mouse demonstrating Cas9/GFP expression limited to the M/TCs. EPL = external plexiform layer, MCL = mitral cell layer. Center, Photomicrograph demonstrating AAV9-DIO-hM4Di(Gi)-mCherry expression limited to the M/TCs (mCherry pseudocolored magenta). Right, Merge, green M/TCs and magenta DREADDs expression. ***B***, Raster plots demonstrating the effect of CNO (DREADDs agonist) on the AP firing activity of a MC without the DREADDs receptor (left) and with the DREADDs receptor (right). Trials progress in the downward direction, gaps indicate 5-min lapses in time. ***C***, Line graph of the AP spike frequency versus time for DREADDs (–)(●) versus DREADDs (+)(■) MCs. The colored bar indicates when CNO was added to the bath solution. ACSF = artificial cerebral fluid (Control bath).

$^{*}p = 0.0041$), without a genotype × time interaction, $p = 0.6117$). For female animals, there was a main effect of time for food intake during the dark cycle (two-way mixed RM ANOVA, main effect of time $F_{(7.468,351)} = 2.422$, $p = 0.0171$) and a genotype × time interaction during the light cycle ($F_{(11,396)} = 1.912$, $p = 0.0363$). *Post hoc* analyses for Figures 16*A–D* indicated no significant differences (all $p \geq 0.05$). Therefore, while the total caloric intake did not change with CRISPR gene targeting (Fig. 11), the manner in which mice consumed food was altered over the course of the 24 h in a sex-dependent and light cycle-dependent way.

Further, we analyzed the relationship between caloric intake and RER. Changes in this relationship could lead to metabolic inflexibility, and drive body weight gain following chronic positive-energy balance (Gonnissen et al., 2013). We focused our analyses on males during the light cycle, because that was the condition wherein RER changes were prominently observed. Both Control and CRISPR animals exhibited a main effect of time (Control = two-way mixed RM ANOVA, time $F_{(5.484,361.9)} = 4.802$, $^{***}p = 0.0002$; CRISPR = time $F_{(5.079,167.6)} = 2.497$, $^{*}p = 0.0321$) and also time × physiological metric interaction (Control = $F_{(11,726)} = 4.616$, $^{****}p < 0.0001$; CRISPR = $F_{(11,363)} = 2.651$, $^{**}p = 0.0028$). However, the relationship of RER and caloric intake was the same in Control versus CRISPR animals (Fig. 16*E*,*F*; three-way mixed RM ANOVA, time × genotype × metric interaction $F_{(11,1089)} = 1.149$, $p = 0.3191$), indicating no CRISPR-mediated difference in such a relationship between caloric intake and RER.

Suppression of M/TCs using inhibitory DREADDs confers a metabolic phenotype

The data above show a correlation between M/TC excitability and whole-body metabolism. We next wanted to investigate whether a decrease in M/TCs excitability could potentially confer an opposite phenotype as that which we observed in the CRISPR mice. We therefore designed an inhibitory DREADDs model by taking advantage of the Tbx21-Cre x Cas9/GFP progeny that would permit selective expression of Cre recombinase and EGFP in the M/TCs (Fig. 17*A*, green channel, 450- to 490-nm excitation). We used direct intracranial injection to deliver Cre-dependent inhibitory DREADDs to the M/TCs of the form AAV9-hSyn-DIO-hM4D(Gi)-mCherry (Fig. 17*A*, red channel, 540- to 590-nm excitation, magenta pseudo-colored, plus green channel merge; yellow co-labeled). The ability of inhibitory DREADDs to suppress neuronal activity is well characterized (Krashes et al., 2011; Vardy et al., 2015; Roth, 2016). As such, we used electrophysiology to confirm that the ligand, CNO, could activate the designer receptor to suppress AP firing in MCs. We performed current-clamp recordings and as shown by the raster plot contained in Figure 17*B*, bath application of CNO was initiated in two representative mice, one a control mouse lacking DREADDs [DREADDS(−), left] and one expressing the designer receptor [DREADDS(+), right]. In the presence of the receptor, CNO completely silenced AP firing with a known slow on rate (Pati et al., 2019) of ~25–30 min (Fig. 17*B*,*C*). In Control animals that lacked the receptor, CNO was ineffective [DREADDS(−)]. Throughout recordings made in two DREADDs mice, we observed that the DREADDs took ~25 min to take effect and hyperpolarized the MCs by nearly 15 mV.

To assess the *in vivo* effect of CNO activation of DREADDs, we examined eight male Tbx21-Cre x Cas9/GFP mice for odor habituation/dishabituation behavior and determined their metabolic profile in the CLAMS. Female mice were not examined because of their insensitivity to DIO. For the behavioral assay, mice were tested twice for odor discrimination as in Figure 9, two weeks apart. We used a randomized crossover design, wherein mice were administered intraperitoneally injection of CNO or saline 30 min before testing. Opposite to what we discovered with the CRISPR mice, CNO-injected DREADDs mice showed a significant reduction in DI versus that of saline-injected controls. CNO-injected DREADDs mice, with suppressed M/TC activity, had poorer olfactory discrimination when the DREADDs were activated [Fig. 18*B*, saline DI = 3.17 ± 1.80 (8) vs CNO DI = 1.66 ± 0.93 (8), ratio paired *t* test, $^{*}p = 0.0420$].

For the metabolic profiling of the Tbx21-Cre x Cas9/GFP DREADDs mice, this same cohort of mice was examined twice in the CLAMS. Mice were metabolically profiled once before DREADDs transduction, and then a second time following recovery from stereotaxic DREADDs surgery. Before DREADDS transduction, we used a randomized crossover design to test the effect of intraperitoneally-administered CNO versus saline. CLAMS-acquired data were assessed for a 4-h window following CNO injection as performed by Inutsuka et al. (2014). In the absence of the DREADDs receptor, CNO had no effect on any of the tested metabolic parameters including food intake, water intake, VO_2, EE, or RER (Extended Data Fig. 19-1, paired *t* test, $p > 0.05$). Following the surgical delivery of the virus, and subsequent expression of the DREADDs receptor, mice were metabolically assessed again. Activation of the DREADDs receptor by CNO induced a reduction in food intake during the dark phase

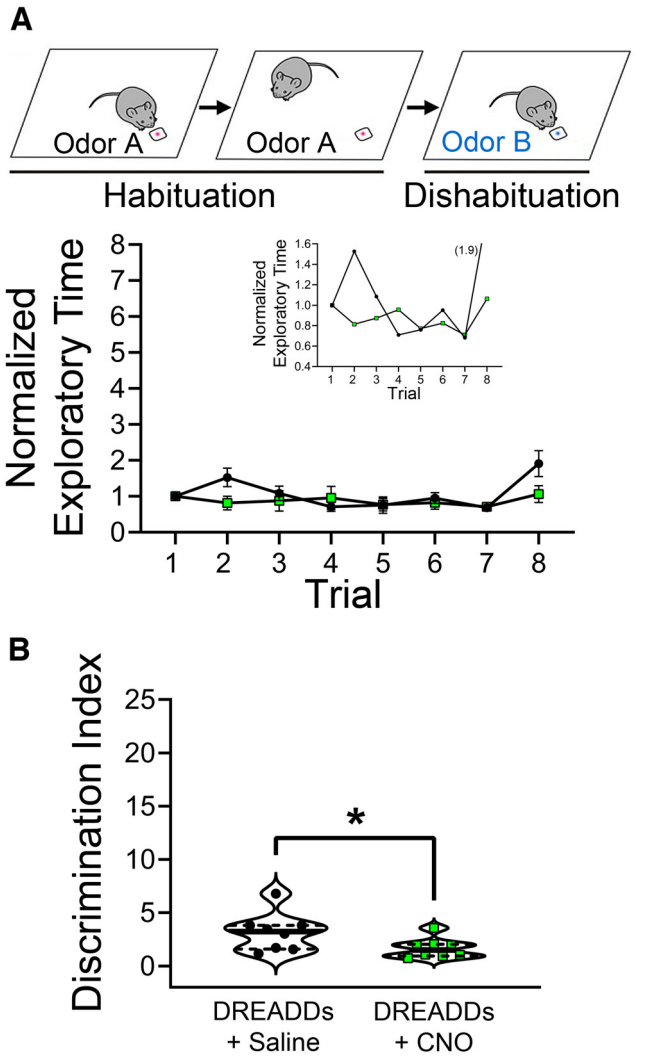

Figure 18. Odor habituation/dishabituation behavior following activation of inhibitory DREADDs. ***A***, Top, Cartoon schematic as in Figure 8. Bottom, Line graph of the mean (±SEM) exploratory time per trial for DREADDS mice injected with Saline (●) versus CNO (■). Inset, Refined scale to visual habituation phase. ***B***, Violin plot of the DI for a population of Saline versus CNO-injected mice tested as in ***A***. DI is calculated as the normalized exploratory time from trial 8 divided by the normalized time from trial 7. Ratio paired *t* test, $^{*}p = 0.0420$.

(Fig. 19*A*, paired *t* test, $^{**}p = 0.0041$, $n = 48$) but not in the light phase (paired *t* test, $p = 0.3908$, $n = 48$). These food intake data are also reported normalized to body weight of the animal (Fig. 20). Unlike that found in the CRISPR animals, that had changes in ingestive behavior, the reduction in caloric intake was not coupled to changes in meal size following CNO activation of the DREADDs receptor (Fig. 19*B*, dark, paired *t* test, $p = 0.1511$, $n = 48$; light, paired *t* test, $p = 0.2559$, $n = 48$). Interestingly, changes in water consumption were noted and oppositely affected across the light phases. Following activation of the DREADDs by CNO, mice consumed less water during the dark phase and more water during the light phase (Fig. 19*C*, dark, paired *t* test, $^{*}p = 0.0462$, $n = 48$; light, paired *t* test, $^{**}p = 0.0019$, $n = 48$).

We next calculated the RER for the mice in response to the injection of CNO versus saline over time, during either the dark or the light phase. There was a main effect of time in both the dark and light phases for RER (Fig. 19*D*, two-way RM ANOVA, dark, time $F_{(3,69)} = 238.0$, $^{****}p < 0.0001$; light, time $F_{(3,69)} = 18.73$, $^{****}p < 0.0001$). In the dark phase, there was a main effect

of CNO injection that transiently reduced RER at the beginning of the phase (Fig. 19*D*, two-way RM ANOVA, drug $F_{(1,23)} = 6.512$, $^{*}p = 0.0178$, Sidak's *post hoc* test, $^{\#\#\#}p = 0.0002$ at 1-h after injection). In the light phase, there was a time × drug interaction where CNO injection caused a delayed increase in RER (Fig. 19*E*, two-way RM ANOVA, time × drug interaction $F_{(3,69)} = 4.057$, $^{*}p = 0.0103$, Sidak's *post hoc* test, $\$\$p = 0.0035$ at 3 h after injection). Unlike the CRISPR mice, activation of DREADDs by CNO evoked changes in both metabolic oxygen consumption (VO_2) and EE (thermogenesis). CNO injection induced a significant reduction in VO_2 during the dark phase (Fig. 19*F*, two-way RM ANOVA, drug $F_{(1,23)} = 10.37$, $^{**}p = 0.0038$, Sidak's *post hoc* test, $^{\#}p = 0.0475$ at 4 h after injection) with no difference observed during the light phase (Fig. 19*G*, two-way RM ANOVA, drug $F_{(1,23)} = 0.4073$, $p = 0.5267$). CNO injection also significantly reduced EE during the dark phase (Fig. 19*H*, two-way RM ANOVA, drug $F_{(1,23)} = 11.80$, $^{**}p = 0.0023$, Sidak's *post hoc* test, $^{\#}p = 0.0424$, $^{\#}p = 0.0242$ at 3 and 4 h after injection, respectively). During the light phase, there was no main effect of drug, but rather a modest time × drug interaction (Fig. 19*I*, two-way RM ANOVA, time × drug interaction $F_{(3,69)} = 2.992$, $^{*}p = 0.0367$, Sidak's *post hoc* test, $\$\$p = 0.0090$ at 2 h after injection), which appeared to slow the rate of decline in thermogenesis noted over the light phase.

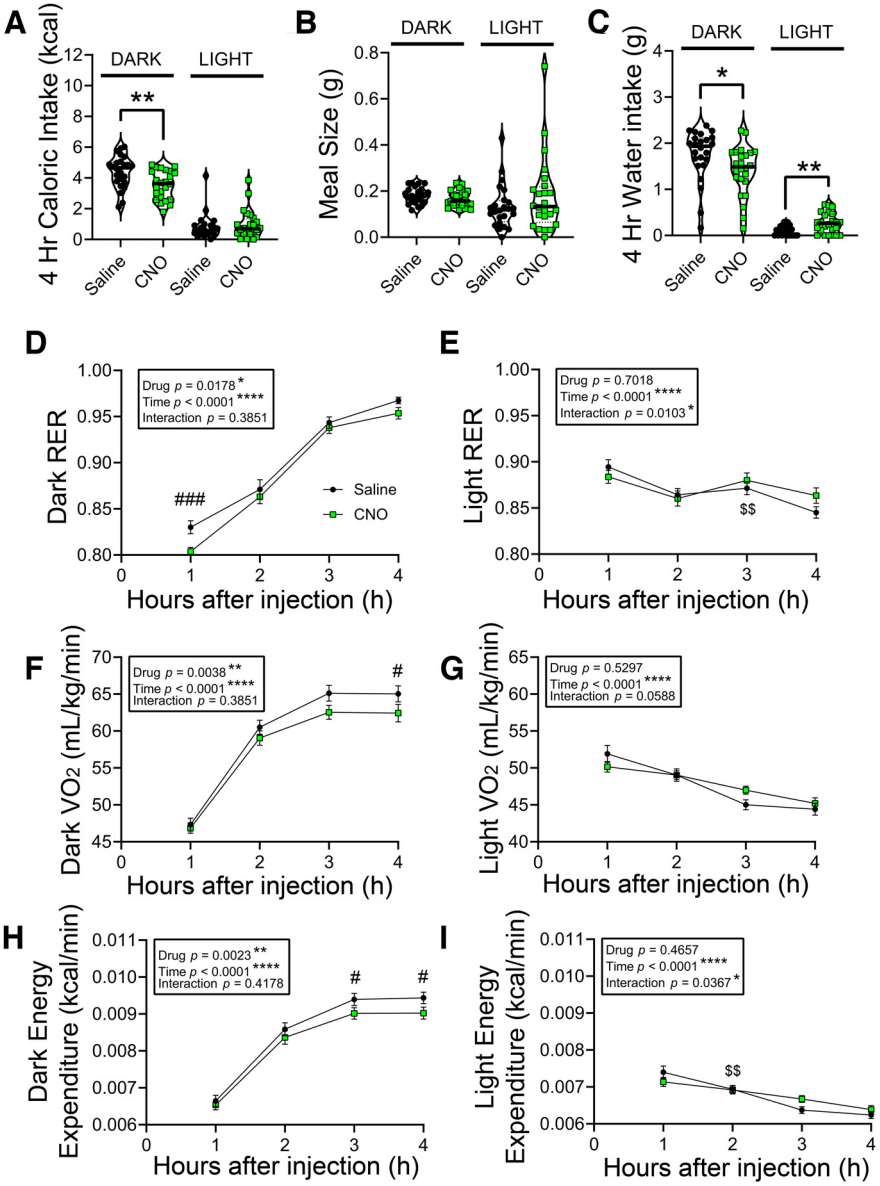

Figure 19. Metabolic assessment of DREADDs male mice with suppressed M/TCs. ***A***, Left, Violin plots comparing (***A***) caloric intake, (***B***) average meal size, and (***C***) water intake for a 4-h interval following saline (●) versus CNO (■) injection of DREADDs mice, analyzed by light phase. Caloric intake, paired *t* test, $^{**}p = 0.0041$. Water intake, paired *t* test, $^{*}p = 0.0462$, $^{**}p = 0.0019$. Line graphs comparing (***D***, ***E***) RER, (***F***, ***G***) oxygen consumption (VO_2), and (***H***, ***I***) EE for a 4-h interval following saline versus CNO injection of DREADDs mice, analyzed by light phase. Two-way RM ANOVA using drug and time as factors. Results of ANOVA in boxes. Sidak's *post hoc* test $\$p < 0.05$, $\$\$p < 0.01$, $\$\$\$p < 0.001$, time × drug interaction compared with 1-h time point. $\#p < 0.05$, main effect of drug within 1-h time point. ***D–I***, Sample sizes are number of metabolic measurements: saline (24), CNO male (24). Additional metabolic parameters compared between Control versus DREADDs mice can be found in tabled form in Extended Data Figure 19-1. The same data reported in ***A***, but normalized to the animal's body weight, can be found in Figure 20.

Discussion

We have demonstrated that altering the excitability of the M/TCs causes both a change in olfactory discrimination and modifies metabolic health in mice. As anticipated, M/TCs with a selective loss of Kv1.3 channels have a less negative RMP, require less current to evoke an AP, and have enhanced spike firing frequency. This effect is likely because of Kv1.3's role as a delayed rectifier channel (Speca et al., 2014). Such an increase in neuronal excitability permits improved odor discrimination, while rendering mice more metabolically healthy when challenged with an obesity-inducing (MHF) diet. Male mice challenged with MHF diet, but also exhibiting enhanced M/TC excitability, show improved glucose clearance, reduction in white adipose tissue, and prevention of fatty liver disease. These are correlated to reduced RER during the light phase, reflective of increased fat metabolism, and a reduction in meal size without changes in total caloric consumption. The improved health and resistance to DIO in CRISPR males does not appear to be attributed to changes in locomotion or thermogenesis. Female mice challenged with MHF diet, but also exhibiting enhanced M/TC excitability, do not demonstrate changes in metabolic health. However, female mice are not basally prone to DIO. Male mice that have transiently-suppressed M/TC activity, induced by targeted chemogenetics, exhibit a reduction in odor discrimination and a concomitant change in metabolism that would drive poorer health outcomes. These mice exhibit reductions in VO_2 and heat generation during the dark phase, and increased fat metabolism (RER) during the dark cycle. They further consume fewer calories during the dark phase and have dark/light phase changes in water intake. Hence, enhancing the

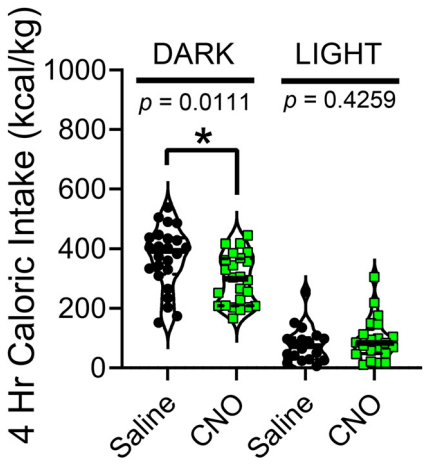

Figure 20. Metabolic assessment of DREADDs male mice with suppressed M/TCs. Same as Figure 19*A* but reported normalized to the body weight of the animal in kilograms.

excitability of M/TCs increases olfactory sensitivity, confers resistance to DIO and insulin resistance, and shifts metabolic substrate utilization. Suppression of M/TC activity, without ablation of sensory input itself, negatively affects metabolic parameters, suggesting an obesogenic phenotype.

M/TCs receive lateral inhibitory input from surrounding glomeruli that respond to the same odor (Christie et al., 2001; Aungst et al., 2003; Wachowiak and Shipley, 2006; Huang et al., 2013). It is possible that exogenously increasing the excitability of M/TCs counters a portion of this inhibition. This is consistent with the combined behavioral and electrophysiological phenotype of the whole-animal Kv1.3−/− mice that have enhanced odor discrimination, reduced odor threshold, and increased excitability of MCs (Fadool et al., 2004, 2011). CRISPR editing of *Kv1.3* in M/TCs produced mice with comparable habituation/dishabituation behaviors to those exhibited by Kv1.3−/− mice. Moreover, both Kv1.3−/− and CRISPR mouse models have significant loss of channel protein as determined by immunoprecipitation/Western blotting.

Biophysical properties of MCs recorded from CRISPR mice have similar properties to those of Kv1.3−/− mice (Fadool et al., 2004, 2011; Mast and Fadool, 2012; Tucker et al., 2013; Thiebaud et al., 2016). Like data reported for our CRISPR mice, MCs recorded from Kv1.3−/− mice have a less negative RMP and enhanced AP frequency. These common properties increase neuronal excitability in both models. We did note subtle differences in AP shape for MCs recorded from our CRISPR mice that we did not observe previously in MCs from Kv1.3−/− mice. Unlike that reported for our CRISPR mice, Kv1.3−/− mice do not exhibit changes in 10–90% rise time or in decay kinetics, whereas APs generated by MCs from the CRISPR show faster rise, shallower rise slope, and slower decay time. These differences could be attributed to the differential mouse strains between these two models, a nonspecific effect of AAV capsid on membrane properties, or differential expression of other voltage-gated ion channels in the Kv1.3−/− mice. Although neither model had measurable changes in Kv1.4, Kv1.5, or Na channel protein, Kv1.3−/− mice did exhibit a compensatory upregulation of Slack/Slick (K_{Na}) channels (Fadool et al., 2004; Lu et al., 2010). Nonetheless, MgTx insensitivity was observed for both Kv1.3−/− and CRISPR mice, signifying loss of Kv1.3 conductances in MCs of both models.

The mechanism through which OB output neurons regulate whole body metabolism is less tangible. Odorant detection and food contact have been demonstrated to modulate the activity of the arcuate nucleus of the hypothalamus (agouti-related neurons; AgRP; Chen et al., 2015; Su et al., 2017). M/TCs indirectly project to the SCN of the hypothalamus via the taenia tecta (disynaptic pathway), and the piriform cortex, amygdala, entorhinal cortex, and anterior olfactory nucleus (trisynaptic pathways; Krout et al., 2002). The SCN is known to regulate metabolism, leptin, insulin, and glucose (Stephan and Zucker, 1972; Butler and Silver, 2009; Rüger and Scheer, 2009). Schneider et al. (2020) recently used transsynaptic viruses to retrogradely label the OB from various subcortical regions: from the arcuate nucleus of the hypothalamus, from reward areas such as the ventral tegmental area and the accumbens nucleus, as well as from the nucleus of the solitary tract (Schneider et al., 2020), which is involved in energy homeostasis and gastric emptying (Abegg et al., 2017). It is possible that the metabolic effects we observed regarding adipose accumulation, resistance to DIO, and substrate utilization (RER) could be accomplished via one or more of these pathways.

Our data show that increased M/TC excitability correlates with a resistance to DIO, and a decrease in excitability may lead to an obesogenic phenotype. Riera et al. (2017) found that Diphtheria toxin-mediated ablation of OSNs confers a resistance to DIO, rather than an obesogenic phenotype, as our results might predict. In their study, ablation of the OSNs caused mice to take significantly longer to find food, and the ablated-OSN mice regularly consumed less high-fat chow than paired controls. One possibility is that the resistance to DIO could be attributed to decreased interest in food and a dysregulation of feeding state (Aimé et al., 2014; Julliard et al., 2017; Al Koborssy et al., 2019), an effect that we did not observe in our CRISPR mice. Our DREADDs mice do consume less chow after suppression of the M/TCs, but this is accompanied by reduction in whole-body metabolic parameters. Additionally, temporary ablation of OSNs leaves M/TCs intact to continually participate in the complex circuitry that regulates whole-body metabolism. Lastly, our cre expression limited genetic alteration to the OB, as demonstrated in Figure 4, which was not the case in the Riera study where expression was observed in the hypothalamus. We judge that by exciting/inhibiting olfactory processing specifically to a central target, we are regulating metabolic control using different pathways than those observed by Riera et al. (2017)

In a series of papers that span 2004–2021, we found that the OB likely played a regulatory role in whole-body metabolism (Fadool et al., 2004; Tucker et al., 2012a; Schwartz et al., 2021). Kv1.3−/− "Super-smeller" mice were resistant to DIO, had irregular ingestive behaviors, and showed increased TEE (Fadool et al., 2004). Interestingly, bilateral olfactory bulbectomy performed on the Kv1.3−/− mice induced anosmia, and reversed metabolic enhancements (Tucker et al., 2012a). Even with the Kv1.3 channel absent in the periphery, the presence of the OB was necessary for resistance to DIO in the Kv1.3−/− mice. Most recently, a pharmacological approach used surgically-implanted osmotic mini-pumps to deliver MgTx-conjugated nanoparticles to the OB (Schwartz et al., 2021). Perfusion of MgTx conferred resistance to DIO, and caused a reduction in RER during the light phase – much like that observed for our CRISPR mice. Since we now report a CRISPR sgRNA that successfully reduces expression of Kv1.3 by 70%, our reported sgRNA sequences may additionally hold promise in treatment models for multiple sclerosis (Judge et al., 1997; Beeton et al., 2001, 2005), in addition to their potential utility to enhance olfactory sensitivity and reduce unwanted weight gain.

Another caveat to our previous studies is that Kv1.3 is highly expressed in the mitochondria of muscle tissue, and regulates GLUT4 trafficking to the membrane (Li et al., 2006). This peripheral effect may have overshadowed the contribution of the OB to metabolism, however, quite interestingly, mitochondrial Kv1.3 is also found in the MC layer. Odor-evoked synaptic transmission in the OB is energetically demanding. The OB shows high expression of GLUT4 for glucose metabolism, and dendrodendritic interactions are associated with a high degree of oxygen consumption (Lecoq et al., 2009). In Kv1.3−/− mice, the size of the mitochondria is notably reduced and is resistant to volume changes from high-fat feeding (Kovach et al., 2016). It is not known whether changes in olfactory Kv1.3 expression can also modify the energetics of synaptic transmission, and not just excitability of output neurons, per se.

We directly demonstrate that the activity level of OB output neurons is not only important for relaying olfactory information, but must project to important metabolic regulation centers to stabilize body weight, glucose clearance, and use of metabolic substrates when challenged with a state of overnutrition. Our results elevate olfactory Kv1.3 as a potential therapeutic target for weight homeostasis or chemosensory deficit, because of its ability to increase M/TC excitability, and concomitantly increase olfactory sensitivity and improve metabolic homeostasis.

References

Abegg K, Hermann A, Boyle CN, Bouret SG, Lutz TA, Riediger T (2017) Involvement of amylin and leptin in the development of projections from the area postrema to the nucleus of the solitary tract. Front Endocrinol 8:324.

Aimé P, Palouzier-Paulignan B, Salem R, Al Koborssy D, Garcia S, Duchamp C, Romestaing C, Julliard AK (2014) Modulation of olfactory sensitivity and glucose-sensing by the feeding state in obese Zucker rats. Front Behav Neurosci 8:326.

Al Koborssy D, Palouzier-Paulignan B, Canova V, Thevenet M, Fadool DA, Julliard AK (2019) Modulation of olfactory-driven behavior by metabolic signals: role of the piriform cortex. Brain Struct Funct 224:315–336.

Aungst JL, Heyward PM, Puche AC, Karnup SV, Hayar A, Szabo G, Shipley MT (2003) Centre–surround inhibition among olfactory bulb glomeruli. Nature 426:623–629.

Balu R, Larimer P, Strowbridge BW (2004) Phasic stimuli evoke precisely timed spikes in intermittently discharging mitral cells. J Neurophysiol 92:743–753.

Bartok A, Toth A, Somodi S, Szanto TG, Hajdu P, Panyi G, Varga Z (2014) Margatoxin is a non-selective inhibitor of human Kv1.3 K+ channels. Toxicon 87:6–16.

Beeton C, Wulff H, Barbaria J, Clot-Faybesse O, Pennington M, Bernard D, Cahalan MD, Chandy KG, Béraud E (2001) Selective blockade of T lymphocyte K+ channels ameliorates experimental autoimmune encephalomyelitis, a model for multiple sclerosis. Proc Natl Acad Sci U S A 98:13942–13947.

Beeton C, Pennington MW, Wulff H, Singh S, Nugent D, Crossley G, Khaytin I, Calabresi PA, Chen CY, Gutman GA, Chandy KG (2005) Targeting effector memory T cells with a selective peptide inhibitor of Kv1.3 channels for therapy of autoimmune diseases. Mol Pharmacol 67:1369–1381.

Bell GA, Fadool DA (2017) Awake, long-term intranasal insulin treatment does not affect object memory, odor discrimination, or reversal learning in mice. Physiol Behav 174:104–113.

Biju KC, Marks DR, Mast TG, Fadool DA (2008) Deletion of voltage-gated channel affects glomerular refinement and odorant receptor expression in the mouse olfactory system. J Comp Neurol 506:161–179.

Butler MP, Silver R (2009) Basis of robustness and resilience in the suprachiasmatic nucleus: individual neurons form nodes in circuits that cycle daily. J Biol Rhythms 24:340–352.

Chejfec G (2001) Clinical diagnosis and management by laboratory methods. Arch Path Lab Med 125:1518–1518.

Chelette BM, Thomas AM, Fadool DA (2019) Long-term obesogenic diet and targeted deletion of potassium channel K_v1.3 have differing effects on voluntary exercise in mice. Physiol Rep 7:e14254.

Chelette BM, Loeven AM, Gatlin DN, Landi Conde DR, Huffstetler CM, Qi M, Fadool DA (2022) Consumption of dietary fat causes loss of olfactory sensory neurons and associated circuitry that is not mitigated by voluntary exercise in mice. J Physiol 600:1473–1495.

Chen TT, Maevsky EI, Uchitel ML (2015) Maintenance of homeostasis in the aging hypothalamus: the central and peripheral roles of succinate. Front Endocrinol (Lausanne) 6:7.

Christie JM, Schoppa NE, Westbrook GL (2001) Tufted cell dendrodendritic inhibition in the olfactory bulb is dependent on NMDA receptor activity. J Neurophysiol 85:169–173.

Cook KK, Fadool DA (2002) Two adaptor proteins differentially modulate the phosphorylation and biophysics of Kv1.3 ion channel by Src kinase. J Biol Chem 277:13268–13280.

Costantini LM, Baloban M, Markwardt ML, Rizzo M, Guo F, Verkhusha VV, Snapp EL (2015) A palette of fluorescent proteins optimized for diverse cellular environments. Nat Commun 6:7670.

De Saint Jan D, Westbrook GL (2007) Disynaptic amplification of metabotropic glutamate receptor 1 responses in the olfactory bulb. J Neurosci 27:132–140.

Deutsch C (2002) Potassium channel ontogeny. Annu Rev Physiol 64:19–46.

Fadool DA, Levitan IB (1998) Modulation of olfactory bulb neuron potassium current by tyrosine phosphorylation. J Neurosci 18:6126–6137.

Fadool DA, Kolling LJ (2020) Role of olfaction for eating behavior. In: The senses: a comprehensive reference, Ed 2 (Fritzsch B, Meyerhof W, eds), pp 675–716. New York: Elsevier.

Fadool DA, Holmes TC, Berman K, Dagan D, Levitan IB (1997) Tyrosine phosphorylation modulates current amplitude and kinetics of a neuronal voltage-gated potassium channel. J Neurophysiol 78:1563–1573.

Fadool DA, Tucker K, Phillips JJ, Simmen JA (2000) Brain insulin receptor causes activity-dependent current suppression in the olfactory bulb through multiple phosphorylation of Kv1.3. J Neurophysiol 83:2332–2348.

Fadool DA, Tucker K, Perkins R, Fasciani G, Thompson RN, Parsons AD, Overton JM, Koni PA, Flavell RA, Kaczmarek LK (2004) Kv1.3 channel gene-targeted deletion produces "Super-Smeller Mice" with altered glomeruli, interacting scaffolding proteins, and biophysics. Neuron 41:389–404.

Fadool DA, Tucker K, Pedarzani P (2011) Mitral cells of the olfactory bulb perform metabolic sensing and are disrupted by obesity at the level of the Kv1.3 ion channel. PLoS One 6:e24921.

Faour M, Magnan C, Gurden H, Martin C (2022) Olfaction in the context of obesity and diabetes: insights from animal models to humans. Neuropharmacology 206:108923.

Foust KD, Nurre E, Montgomery CL, Hernandez A, Chan CM, Kaspar BK (2009) Intravascular AAV9 preferentially targets neonatal neurons and adult astrocytes. Nat Biotechnol 27:59–65.

Gonnissen HKJ, Hulshof T, Westerterp-Plantenga MS (2013) Chronobiology, endocrinology, and energy- and food-reward homeostasis. Obes Rev 14:405–416.

Haddad R, Lanjuin A, Madisen L, Zeng H, Murthy VN, Uchida N (2013) Olfactory cortical neurons read out a relative time code in the olfactory bulb. Nat Neurosci 16:949–957.

Holmes TC, Fadool DA, Levitan IB (1996) Tyrosine phosphorylation of the Kv1.3 potassium channel. J Neurosci 16:1581–1590.

Huang L, Garcia I, Jen HI, Arenkiel BR (2013) Reciprocal connectivity between mitral cells and external plexiform layer interneurons in the mouse olfactory bulb. Front Neural Circ 7:32.

Huang Z, Hoffman CA, Chelette BM, Thiebaud N, Fadool DA (2018) Elevated anxiety and impaired attention in super-smeller, Kv1.3 knockout mice. Front Behav Neurosci 12:49.

Imamura F, Ito A, LaFever B (2020) Subpopulations of projection neurons in the olfactory bulb. Front Neural Circ 14:58.

Inutsuka A, Inui A, Tabuchi S, Tsunematsu T, Lazarus M, Yamanaka A (2014) Concurrent and robust regulation of feeding behaviors and metabolism by orexin neurons. Neuropharmacol 85:451–460.

Jan LY, Jan NJ (1994) Potassium channels and their evolving gates. Nature 371:119–122.

Jin S, Diano S (2018) Mitochondrial dynamics and hypothalamic regulation of metabolism. Endocrinology 159:3596–3604.

Jones S, Zylberberg J, Schoppa N (2020) Cellular and synaptic mechanisms that differentiate mitral cells and superficial tufted cells into parallel output channels in the olfactory bulb. Front Cell Neurosci 14:614377.
Judge SIV, Yeh JZ, Mannie MD, Seifert LP, Paterson PY (1997) Potassium channel blockers inhibit adoptive transfer of experimental allergic encephalomyelitis by myelin-basic-protein-stimulated rat T lymphocytes. J Biomed Sci 4:169–178.
Julliard AK, Al Koborssy D, Fadool DA, Palouzier-Paulignan B (2017) Nutrient sensing: another chemosensitivity of the olfactory system. Front Physiol 8:468.
Kaczmarek L (2006) Non-conducting functions of voltage-gated ion channels. Nat Rev Neurosci 7:761–771.
Kovach CP, Al Koborssy D, Huang Z, Chelette BM, Fadool JM, Fadool DA (2016) Mitochondrial ultrastructure and glucose signaling pathways attributed to the Kv1.3 ion channel. Front Physiol 7:178.
Krashes MJ, Koda S, Ye CP, Rogan SC, Adams AC, Cusher DS, Maratos-Flier E, Roth BL, Lowell BB (2011) Rapid, reversible activation of AgRP neurons drives feeding behavior in mice. J Clin Invest 121:1424–1428.
Krimer LS, Goldman-Rakic PS (1997) An interface holding chamber for anatomical and physiological studies of living brain slices. J Neurosci Meth 75:55–58.
Krout KE, Kawano J, Mettenleiter TC, Loewy AD (2002) CNS inputs to the suprachiasmatic nucleus of the rat. Neurosci 110:73–92.
Kuczewski N, Fourcaud-Trocmé N, Savigner A, Thevenet M, Aimé P, Garcia S, Duchamp-Viret P, Palouzier-Paulignan B (2014) Insulin modulates network activity in olfactory bulb slices: impact on odour processing. J Physiol 592:2751–2769.
Kupper J (1998) Functional expression of GFP-tagged Kv1.3 and Kv1.4 channels in HEK 293 cells. Eur J Neurosci 10:3908–3912.
Lecoq J, Tiret P, Najac M, Shepherd GM, Greer CA, Charpak S (2009) Odor-evoked oxygen consumption by action potential and synaptic transmission in the olfactory bulb. J Neurosci 29:1424–1433.
Li Y, Wang P, Xu J, Desir GV (2006) Voltage-gated potassium channel Kv1.3 regulates GLUT4 trafficking to the plasma membrane via a Ca2+-dependent mechanism. Am J Physiol Cell Physiol 290:C345–C351.
Lu S, Das P, Fadool DA, Kaczmarek LK (2010) The slack sodium-activated potassium channel provides a major outward current in olfactory neurons of Kv1.3-/- super-smeller mice. J Neurophysiol 103:3311–3319.
Lusk G, Bois EF Du (1924) On the constancy of the basal metabolism. J Physiol 59:213–216.
Manvich DF, Webster KA, Foster SL, Farrell MS, Ritchie JC, Porter JH, Weinshenker D (2018) The DREADD agonist clozapine N-oxide (CNO) is reverse-metabolized to clozapine and produces clozapine-like interoceptive stimulus effects in rats and mice. Sci Rep 8:3840.
Marks DR, Fadool DA (2007) Post-synaptic density perturbs insulin-induced Kv1.3 channel modulation via a clustering mechanism involving the SH3 domain. J Neurochem 103:1608–1627.
Marks DR, Tucker K, Cavallin MA, Mast TG, Fadool DA (2009) Awake intranasal insulin delivery modifies protein complexes and alters memory, anxiety, and olfactory behaviors. J Neurosci 29:6734–6751.
Marom S, Goldstein S, Kupper J, Levitan I (1993) Mechanism and modulation of inactivation of the Kv3 potassium channel. Recept Channels 1:81–88.
Marty L, Bentivegna H, Nicklaus S, Monnery-Patris S, Chambaron S (2017) Non-conscious effect of food odors on children's food choices varies by weight status. Front Nutr 4:16.
Mast TG, Fadool DA (2012) Mature and precursor brain-derived neurotrophic factor have individual roles in the mouse olfactory bulb. PLoS One 7:e31978.
Murphy C, Vertrees R (2017) Sensory functioning in older adults: relevance for food preference. Curr Opin Food Sci 15:56–60.
Murphy FA, Tucker K, Fadool DA (2001) Sexual dimorphism and developmental expression of signal-transduction machinery in the vomeronasal organ. J Comp Neurol 432:61–74.
Nickell WT, Shipley MT, Behbehani MM (1996) Orthodromic synaptic activation of rat olfactory bulb mitral cells in isolated slices. Brain Res Bull 39:57–62.
Palouzier-Paulignan B, Lacroix M-C, Aime P, Baly C, Caillol M, Congar P, Julliard AK, Tucker K, Fadool DA (2012) Olfaction under metabolic influences. Chem Senses 37:769–797.
Pati S, Salvi SS, Kallianpur M, Vaidya B, Banerjee A, Maiti S, Clement JP, Vaidya VA (2019) Chemogenetic activation of excitatory neurons alters hippocampal neurotransmission in a dose-dependent manner. eNeuro 6: ENEURO.0124-19.2019.
Riera CE, Tsaousidou E, Halloran J, Follett P, Hahn O, Pereira MMA, Ruud LE, Alber J, Tharp K, Anderson CM, Brönneke H, Hampel B, Filho CDM, Stahl A, Brüning JC, Dillin A (2017) The sense of smell impacts metabolic health and obesity. Cell Metab 26:198–211.
Roth BL (2016) DREADDs for neuroscientists. Neuron 89:683–694.
Rothermel M, Brunert D, Zabawa C, Díaz-Quesada M, Wachowiak M (2013) Transgene expression in target-defined neuron populations mediated by retrograde infection with adeno-associated viral vectors. J Neurosci 33:15195–15206.
Rüger M, Scheer D (2009) Effects of circadian disruption on cardiometabolic system. Rev Endocr Metab Disord 10:245–260.
Sanjana N, Shalem O, Zhang F (2014) Improved vectors and genome-wide libraries for CRISPR screening. Nat Methods 11:783–784.
Schneider NY, Chaudy S, Epstein AL, Viollet C, Benani A, Pénicaud L, Grosmaître X, Datiche F, Gascuel J (2020) Centrifugal projections to the main olfactory bulb revealed by transsynaptic retrograde tracing in mice. J Comp Neurol 528:1805–1819.
Schoppa NE, Westbrook GL (2001) Glomerulus-specific synchronization of mitral cells in the olfactory bulb. Neuron 31:639–651.
Schwartz AB, Kapur A, Wang W, Huang Z, Fardone E, Palui G, Mattoussi H, Fadool DA (2017) Margatoxin-bound quantum dots as a novel inhibitor of the voltage-gated ion channel Kv1.3. J Neurochem 140:404–420.
Schwartz AB, Kapur A, Huang Z, Anangi R, Spear JM, Stagg S, Fardone E, Dekan Z, Rosenberg JT, Grant SC, King GF, Mattoussi H, Fadool DA (2021) Olfactory bulb-targeted quantum dot (QD) bioconjugate and Kv1.3 blocking peptide improve metabolic health in obese male mice. J Neurochem 157:1876–1896.
Short SM, Wachowiak M (2019) Temporal dynamics of inhalation-linked activity across defined subpopulations of mouse olfactory bulb neurons imaged in vivo. eNeuro 6:ENEURO.0189-19.2019.
Spear JM, Al Koborssy D, Schwartz AB, Johnson AJ, Audhya A, Fadool DA, Stagg SM (2015) Kv1.3 contains an alternative C-terminal ER exit motif and is recruited into COPII vesicles by Sec24a. BMC Biochem 16:16.
Speca DJ, Ogata G, Mandikian D, Bishop HI, Wiler SW, Eum K, Wenzel HJ, Doisy ET, Matt L, Campi KL, Golub MS, Nerbonne JM, Hell JW, Trainor BC, Sack JT, Schwartzkroin PA, Trimmer JS (2014) Deletion of the Kv2.1 delayed rectifier potassium channel leads to neuronal and behavioral hyperexcitability. Genes Brain Behav 13:394–408.
Stephan FK, Zucker I (1972) Rat drinking rhythms: central visual pathways and endocrine factors mediating responsiveness to environmental illumination. Physiol Behav 8:315–326.
Su Z, Alhadeff AL, Betley JN (2017) Nutritive, post-ingestive signals are the primary regulators of AgRP neuron activity. Cell Rep 21:2724–2736.
Thiebaud N, Johnson MC, Butler JL, Bell GA, Ferguson KL, Fadool AR, Fadool JC, Gale AM, Gale DS, Fadool DA (2014) Hyperlipidemic diet causes loss of olfactory sensory neurons, reduces olfactory discrimination, and disrupts odor-reversal learning. J Neurosci 34:6970–6984.
Thiebaud N, Llewellyn-Smith IJ, Gribble F, Reimann F, Trapp S, Fadool DA (2016) The incretin hormone glucagon-like peptide 1 increases mitral cell excitability by decreasing conductance of a voltage-dependent potassium channel. J Physiol 594:2607–2628.
Tucker K, Fadool DA (2002) Neurotrophin modulation of voltage-gated potassium channels in rat through TrkB receptors is time and sensory experience dependent. J Physiol 542:413–429.
Tucker K, Overton JM, Fadool DA (2008) Kv1.3 gene-targeted deletion alters longevity and reduces adiposity by increasing locomotion and metabolism in melanocortin-4 receptor-null mice. Int J Obes (Lond) 32:1222–1232.
Tucker K, Cavallin MA, Jean-Baptiste P, Biju KC, Overton JM, Pedarzani P, Fadool DA (2010) The olfactory bulb: a metabolic sensor of brain insulin and glucose concentrations via a voltage-gated potassium channel. Results Probl Cell Differ 52:147–157.
Tucker K, Overton JM, Fadool DA (2012a) Diet-induced obesity resistance of Kv1.3−/− mice is olfactory bulb dependent. J Neuroendocrinol 24:1087–1095.
Tucker KR, Godbey SJ, Thiebaud N, Fadool DA (2012b) Olfactory ability and object memory in three mouse models of varying body weight, metabolic hormones, and adiposity. Physiol Behav 107:424–432.
Tucker K, Cho S, Thiebaud N, Henderson MX, Fadool DA (2013) Glucose sensitivity of mouse olfactory bulb neurons is conveyed by a voltage-gated potassium channel. J Physiol 591:2541–2561.

Upadhyay SK, Eckel-Mahan KL, Mirbolooki MR, Tjong I, Griffey SM, Schmunk G, Koehne A, Halbout B, Iadonato S, Pedersen B, Borrelli E, Wang PH, Mukherjee J, Sassone-Corsi P, Chandy KG (2013) Selective Kv1.3 channel blocker as therapeutic for obesity and insulin resistance. Proc Natl Acad Sci U S A 110:E2239–E2248.

Vardy E, et al. (2015) A new DREADD facilitates the multiplexed chemogenetic interrogation of behavior. Neuron 86:936–946.

Vélez P, Schwartz AB, Iyer SR, Warrington A, Fadool DA (2016) Ubiquitin ligase Nedd4-2 modulates Kv1.3 current amplitude and ion channel protein targeting. J Neurophysiol 116:671–685.

Wachowiak M, Shipley MT (2006) Coding and synaptic processing of sensory information in the glomerular layer of the olfactory bulb. Semin Cell Dev Biol 17:411–423.

Williams TD, Chambers JB, Henderson RP, Rashotte ME, Overton JM (2002) Cardiovascular responses to caloric restriction and thermoneutrality in C57BL/6J mice. Am J Physiol Regul Integr Comp Physiol 282:R1459–R1467.

Xu J, Koni PA, Wang P, Li G, Kaczmarek L, Wu Y, Li Y, Flavell RA, Desir GV (2003) The voltage-gated potassium channel Kv1.3 regulates energy homeostasis and body weight. Hum Mol Genet 12:551–559.

Xu J, Wang P, Li Y, Li G, Kaczmarek LK, Wu Y, Koni PA, Flavell RA, Desir GV (2004) The voltage-gated potassium channel Kv1.3 regulates peripheral insulin sensitivity. Proc Natl Acad Sci U S A 101:3112–3117.

Yardeni T, Eckhaus M, Morris HD, Huizing M, Hoogstraten-Miller S (2011) Retro-orbital injections in mice. Lab Anim (NY) 40:155–160.

Yellen G (2002) The voltage-gated potassium channels and their relatives. Nature 419:35–42.

Zeppilli S, Ackels T, Attey R, Klimpert N, Ritola KD, Boeing S, Crombach A, Schaefer AT, Fleischmann A (2021) Molecular characterization of projection neuron subtypes in the mouse olfactory bulb. Elife 10:e65445.

Zhang H, Yang B, Mu X, Ahmed SS, Su Q, He R, Wang H, Mueller C, Sena-Esteves M, Brown R, Xu Z, Gao G (2011) Several rAAV vectors efficiently cross the blood-brain barrier and transduce neurons and astrocytes in the neonatal mouse central nervous system. Mol Ther 19:1440–1448.